A quantitative analysis of the ignition characteristics of fine iron particles

Document status and date:
Published: 01/06/2022

Document Version:
Publisher's PDF, also known as Version of Record (includes final page, issue and volume numbers)

Please check the document version of this publication:

• A submitted manuscript is the version of the article upon submission and before peer-review. There can be important differences between the submitted version and the official published version of record. People interested in the research are advised to contact the author for the final version of the publication, or visit the DOI to the publisher's website.
• The final author version and the galley proof are versions of the publication after peer review.
• The final published version features the final layout of the paper including the volume, issue and page numbers.
Link to publication

A quantitative analysis of the ignition characteristics of fine iron particles

XiaoCheng Mi [a,b,*], Aki Fujinawa [a], Jeffrey M. Bergthorson [a]

[a] Department of Mechanical Engineering, McGill University, Montreal H3A 0C3, Canada
[b] Department of Mechanical Engineering, Eindhoven University of Technology, Eindhoven 5600 MB, the Netherlands

ARTICLE INFO

ABSTRACT

Ignition of iron particles in an oxidizing environment marks the onset of self-sustained combustion. The objective of the current study is to quantitatively examine the ignition characteristics of fine iron particles (i.e., 1μm- to 100μm-sized) governed by the kinetics of solid-phase iron oxidation. The oxidation rates are inversely proportional to the thickness of the oxide layer (i.e., following a parabolic rate law) and calibrated using the experimentally measured growth of iron-oxide layers over time. Steady-state (i.e., Semenov's analysis) and unsteady analysis have been performed to probe the dependence of the critical gas temperature required to trigger a thermal runaway (namely, the ignition temperature T_{ign}) on particle size, initial thickness of oxide layer, inert gas species, radiative heat loss, and the collective heating effect in a suspension of particles. Both analyses indicate that T_{ign} depends on δ_0, i.e., the ratio between the initial oxide layer thickness and particle size, regardless of the absolute size of the particle. The unsteady analysis predicts that, for $\delta_0 \lesssim 0.003$, T_{ign} becomes independent of δ_0. Under standard conditions in air, T_{ign} is approximately 1080 K for any particle size greater than 5μm. The ignition temperature decreases as the thermal conductivity of the oxidizing gas decreases. Radiative heat loss has a minor effect on T_{ign}. The collective effect of a suspension of iron particles in reducing T_{ign} is demonstrated. The transition behavior between kinetic-controlled and external-diffusion-controlled combustion regimes of an ignited iron particle is systematically examined. The influences of initial oxide-layer thickness and particle temperature on the ignition delay time, τ_{ign}, of iron particles are parametrically probed. A d^2-law scaling between τ_{ign} and particle size is identified. Possible sources of inaccuracy are discussed.

1. Introduction

Iron is an excellent fuel for long-term storage and long-distance transport of clean energy owing to its carbon-free nature, high energy density, and potential for non-volatile combustion in air [1–3]. For developing practical energy-conversion technologies based on iron fuel, a better understanding of the fundamentals underlying the combustion process of fine (i.e., micron- to hundreds-of-micron-sized) iron particles at elevated temperatures is required. The full oxidation process of an iron particle in a combustion system consists of three major stages: (1) Preheating and ignition leading to a thermal runaway; (2) a rapid oxidation process of a molten droplet at elevated temperatures until iron is completely oxidized; (3) a slow further oxidation process of the lower oxidized products, i.e., from FeO or Fe_3O_4 to Fe_2O_3, upon cooling. To design a real-world combustion device of iron particles, quantitative answers are required for the following questions: (A) Under what conditions can iron particles be ignited? (B) How to ensure a non-volatile combustion of molten iron droplets? (C) What are the rates of energy release during the rapid and slow iron oxidation processes? To answer these questions, we need to better identify the rate-controlling mechanisms among a complex of physicochemical processes in the different stages of iron combustion, including oxygen diffusion in the gas, oxygen absorption at the particle surface, phase change and dissociative evaporation of iron and its oxides, solid- and liquid-phase kinetics of iron oxidation, and heat exchange between particles and the ambient gas. Both experimental and theoretical endeavors are required for this exploration.

Prior to the research campaigns on fine iron particles, knowledge of iron combustion has mostly been acquired from experimental investigations on the growth of solid iron-oxide scales

---

* Corresponding author.
E-mail addresses: x.c.mi@tue.nl, xiaocheng.mi@mail.mcgill.ca (X. Mi).

in air [4–8] and iron rod combustion in high pressure oxygen [9–15]. Metallurgical studies [4,5] dated in the 1950s demonstrated that the growth of solid-phase iron oxides on a specimen of pure iron at a steady temperature follows a parabolic rate law, namely, with a rate inversely proportional to the thickness of the oxide scale. This finding agrees well with the prediction of Wagner's theory [16] asserting that the rate of solid-phase metal oxidation is controlled by the lattice diffusion of ions across the oxide scale [17]. Quantitatively accurate kinetics for solid-phase iron oxidation can be determined from these experimental results.

The combustion complex of a mm-diameter iron rod consists of a molten droplet of iron and iron oxides attached to a reaction front that melts and propagates into the solid rod [9]. Dreizin [18] elucidated that the burning rate of an iron rod can be either limited by the iron oxidation kinetics at sufficiently high gas temperatures [11,12] or the incorporation rate of gaseous oxygen at low gas temperatures [9,19]. Recent studies by Muller *et al.* [14,15] reveal more details of the molten mixture formed on the top of a laser-ignited iron rod. A spatially non-uniform distribution of molten iron, oxides, and gas bubbles inside the droplet was identified [15]. A subsequent modeling work [20] further describes the complex thermo-fluid processes within this molten-phase mixture controlling the burning rate of an iron rod. Alas, quantitatively useful information to answer the aforeposed questions for iron-particle combustion is mostly masked by the intrinsic complexity of iron-rod combustion.

Over the past two decades, the state-of-the-art understanding in the combustion of fine iron particles has been advanced by researchers around the globe. This collective effort has, however, been mainly focused on experimentally examining [21–28] and qualitatively modeling [29–34] the macroscopic observables of flame propagation in a dispersion of iron particles in an oxidizing gas. Although a few recent experimental studies [35–38] attempt to monitor the combustion process of individual iron particles, in situ measurements of particle temperature and composition have not yet been *extensively* obtained. Thus, the detailed rate-controlling mechanisms of iron-particle combustion, especially for a molten droplet, remain elusive. Without a physics-based, quantitatively reliable model for calculating the energy release rate of an iron particle, the development of high-fidelity simulations of large-scale combustion systems is baseless despite the sophistication achieved in modeling other components of the problem.

This paper reports an effort in seeking a quantitative answer to the aforementioned Question (A) with regard to the *ignition characteristics* of fine iron particles. To ignite an iron particle means that a set of critical conditions (e.g., gas or particle temperature) is satisfied to trigger a thermal runaway—the rate of energy release due to iron oxidation exceeds the rate of heat loss to the surrounding. There is yet no experimental measurement of the critical particle or gas temperature required for triggering thermal runaway (referred to as "ignition temperature in the remainder of this paper") of an isolated particle, or a suspension of iron particles, in a flame. The experimental data of iron ignition temperature in the literature were obtained for suspensions and precipitated beds of fine iron powders [39,40] and mm- to cm-sized iron or steel specimens [41–43]. These data, as partly summarized by Breiter *et al.* [44], are widely scattered owing to the difference in experimental conditions, specimen properties and morphologies, and definition of "ignition temperature". The experimental measurement reported by Grosse and Conway [41] and Bolobov [43] are perhaps the closest to the herein defined ignition temperature. In Grosse and Conways study [41], a 10-g-weighted specimen of iron was placed in an Alundum crucible and heated to a designated temperature in an argon atmosphere by an electric furnace, and then, a flow of oxygen was fed to the top of the crucible. This procedure was repeated with an incremented temperature until an event of

thermal runaway was detected by visual observation. An ignition temperature of 1203 ± 10 K was obtained. A similar procedure was followed by Bolobov [43] to determine the ignition temperature of a $5 \times 5 \times 0.5$ mm low-carbon steel foil. The specimens were heated in vacuum to a designated temperature before supplying oxygen. The event of a thermal runaway was detected as an abrupt increase in the temporal record of specimen temperature. An ignition temperature of 1233 ± 20 K, independent of ambient oxygen concentration, was found. Both of these experimental results of ignition temperature are significantly below the melting point of FeO, i.e., 1650K, indicating that the ignition process occurs when a particle remains completely in solid phase.[1]

Khaikin [45] proposed a generic ignition model for reactive metal particles considering the obstructing effect of an oxide layer on the reaction rate, but did not apply it for quantitatively estimating the ignition temperature of iron particles. A quantitative model was developed by Bolobov and Podlevskikh [46] to explain the ignition characteristics of a low-carbon steel foil as experimentally probed in Ref. [43]. Despite some ambiguity in the kinetic parameters for iron oxidation, the ignition temperatures predicted by Bolobov and Podlevskikhs model [46] are fairly close to the experimental results with a discrepancy less than 50 K. The current study aims to develop a model to quantitatively capture the ignition characteristics of fine iron particles. To this end, a physics-based kinetic model of solid-phase iron oxidation—a parabolic rate law reflecting that the oxidation rate is controlled by the lattice diffusion of Fe cations through oxide layers—is considered in the current ignition model. The values of the kinetic parameters were calibrated against the experimental measurement of growth rates of iron-oxide scales over a temperature range from 973 K to 1523 K obtained by Païdassi [4]. Using this model, the effects of initial particle size, initial oxide layer thickness, inert gas species, radiative heat loss, and collective heating in a particulate suspension on the ignition characteristics of iron particles are examined. The model prediction of ignition temperature is compared with the experimental results of Grosse and Conway [41] and Bolobov [43]. The transition behavior between kinetic-controlled and external-diffusion-controlled combustion regimes and the ignition delay times of iron particles are further examined. The possible sources of error of this model are also discussed.

2. Iron oxidation kinetic model

2.1. Physics underlying solid-phase iron oxidation

Microscopic cross-section views of a solid-phase oxide scale grown on iron under isothermal conditions (over a range in temperature from 973 K to 1523 K) in air were first obtained by Païdassi in the 1950s [4]. Figure 1(a) is a sample image from Ref. [4] showing that an iron-oxide scale consists of three compact layers of hematite (Fe_2O_3), magnetite (Fe_3O_4), and wüstite (FeO) stacked from the gas-oxide interface to the oxide-iron interface. The relative thicknesses of the Fe_2O_3, Fe_3O_4, and FeO layers with respect to the total thickness of the oxide scale are 1%, 4%, and 95%, respectively. As conceptually illustrated in Fig. 1(b), for a compact oxide film (i.e., without cracks or grain boundaries to facilitate oxygen transport to the iron core), solid-phase iron oxidation consists of the following processes:

1. Diffusion of oxygen (O_2) molecules from the bulk gas to the gas-oxide interface.
2. Incorporation of oxygen into the oxide scale (i.e., a dissociative absorption of O_2 molecules as oxygen anions O^{2-}).

---

[1] The melting points of Fe, Fe_2O_3, and Fe_3O_4, i.e., 1811K, 1838K, and 1870K, respectively, are all greater than that of FeO.
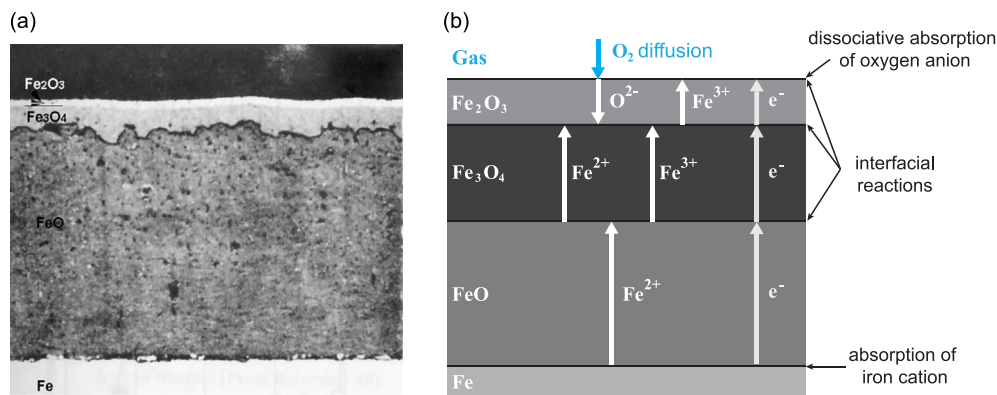
Fig. 1. (a) A sample cross-section view of a multilayered oxide scale grown on iron as shown by Païdassi [4]; (b) a schematic illustration showing the key processes underlying solid-phase iron oxidation.

3. Absorption of iron into the oxide film as iron cations.
4. Diffusion of ions and electrons through the oxide scale.
5. Reactions at FeO-Fe$_3$O$_4$, Fe$_3$O$_4$-Fe$_2$O$_3$, and Fe$_2$O$_3$-O$_2$ interfaces.

At relatively low temperatures, the diffusion of oxygen in the gas phase (Process 1) is much more rapid than the kinetic processes (2 to 5) in the solid phase. As the temperature of the particle increases, the solid-phase kinetics become increasingly rapid and thus, the external diffusion of oxygen becomes the rate-limiting process. In this analysis, the oxidation rate is considered to be only controlled by the solid-phase kinetics for determining the critical conditions for particle ignition, i.e., the critical temperature required to trigger thermal runaway, in Sects. 5.1–5.5; a *switch-type* reaction-rate model, considering the transition from kinetic- to external-diffusion-controlled combustion, is used describe the ignition behavior of iron particles beyond the critical temperature for thermal runaway, in Sects. 5.6 and 5.7.

For a sufficiently thick oxide scale, the growth rate of each layer is controlled by the diffusion of ions subjected to the equilibrium activities of Fe and O at the interfaces [47]. Considering the fact that the transport of electrons and the establishment of local equilibria at the interfaces are significantly more rapid than the diffusion of ions across the oxide layers, Wagner's theory [16] relates the oxide growth rate to the diffusivity of ions. Since Fe cations are significantly more mobile in FeO and Fe$_3$O$_4$ layers than O anions due to a large size of O anion (1.4 Å) [48], the growth of oxide film is predominantly governed by the outward diffusion of Fe cations [7,49]. The growth of the FeO layer is the most rapid due to the fact that the diffusion coefficient of Fe cations in FeO is greater than that in Fe$_3$O$_4$ or Fe$_2$O$_3$. Such a diffusion-controlled growth follows a parabolic rate law,

$$\frac{dX_i}{dt} = \frac{k_{p,i}}{X_i} \tag{1}$$

where X_i is the thickness of an oxide layer, $k_{p,i}$ is the parabolic rate constant, and i is the index of each oxide layer. Yurek *et al.* [6] and Garnaud and Rapp [8] extended Wagner's theory to show that the growth of a multilayered oxide film on iron follows a parabolic rate law governed by the diffusion coefficients of Fe in FeO and Fe$_3$O$_4$. It is of importance to note that, as revealed by Goursat and Smeltzer [50], the oxidation kinetics of FeO is independent of ambient oxygen concentration over a temperature range (at least) from 1073 K to 1273 K for a partial pressure of O$_2$ (p_{O_2}) above 4×10^{-4} atm. As the activities of Fe and O at the Fe-FeO, FeO-Fe$_3$O$_4$, and Fe$_3$O$_4$-Fe$_2$O$_3$ interfaces are fixed by the phase equilibria, the growth of FeO and Fe$_3$O$_4$ are barely affected by the ambient O$_2$ concentration [51]. In this analysis, the kinetic rates of FeO and Fe$_3$O$_4$ formation are assumed to be independent of ambient

O$_2$ concentration as long as p_{O_2} is greater than zero. The implication of this assumption on the ignition process—the transition from a kinetic-controlled combustion to an O$_2$-diffusion-controlled (also referred to as external-diffusion-controlled) combustion—of an iron particle is discussed in Sect. 5.6.

Since the growth of the Fe$_2$O$_3$ layer is significantly slower in comparison to the growth of the FeO and Fe$_3$O$_4$ layers, the energy release due to the formation Fe$_2$O$_3$ is negligible. The formation of this thin Fe$_2$O$_3$ layer is thus neglected in the current analysis. It is, however, of importance to understand the role played by the hematite layer on the formation of the inner oxidized layers. There is experimental evidence [52,53] indicating that the formation of Fe$_2$O$_3$ is due to both an outward diffusion of Fe cations and an inward diffusion of O anions at comparable rates (as illustrated in Fig. 1(b)), possibly along cracks in the hematite layer. Goursat and Smeltzer [50] showed that the Fe$_2$O$_3$ layer formed upon the Fe$_3$O$_4$ layer is a dense "forest" of whiskers and platelets. The growth rate of this irregular hematite layer adapts to the ambient O$_2$ concentration, establishing an equilibrium at the Fe$_3$O$_4$-Fe$_3$O$_2$ interface, and thus, making the growth rates of FeO and Fe$_3$O$_4$ independent of O$_2$ concentration.

2.2. Calibration of the kinetic model

The experimental data of Païdassi [4] reveal that, at a steady temperature, the thickness of each oxide layer X_i increases with square root of time $\sqrt{t}$ at a constant rate, indeed following a parabolic rate law. The parabolic rate constant k_i can be measured as the slope of the fitted line to the experimental data of X_i as a function of $\sqrt{t}$ at each temperature, i.e., $X_i = k_i\sqrt{t} + X_{i,0}$, as reported in Table 1 of Ref. [4]. Note that k_i can be converted to the rate constant $k_{p,i}$ in Eq. 1 via the relation as follows:

$$k_{p,i} = \frac{k_i^2}{2} \tag{2}$$

The natural logarithmic values of the experimental data of $k_{p,i}$ for the growth of total oxide film thickness (blue diamond), FeO layer thickness (red square), and Fe$_3$O$_4$ layer thickness (black circle) are plotted in Fig. 2 as a function of the reciprocal of temperature, $1/T$. These data points demonstrate a linear regression, i.e., the parabolic rate constant increases exponentially with temperature, indicating that the diffusion of Fe cations in the oxide layers is an activated process. The temperature dependence of $k_{p,i}$ can be described by an Arrhenius function as follows,

$$k_{p,i}(T) = k_{0,i}\text{Exp}\left(\frac{-T_{a,i}}{T}\right) \tag{3}$$

wherein the values of pre-exponential factor $k_{0,i}$ and activation temperature $T_{a,i}$ for the growth of FeO and Fe$_3$O$_4$ layers can be
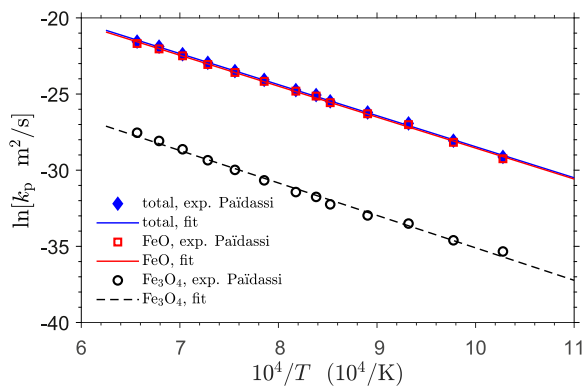
Fig. 2. The natural logarithmic values of the experimental data of $k_{p,i}$ for the growth of total oxide scale thickness (blue diamond), FeO layer thickness (red square), and Fe_3O_4 layer thickness (black circle) plotted as a function of the reciprocal of temperature, $1/T$, and a fitting line showing a linear regression of the corresponding data. Note that the FeO and total oxide growth rates are effectively equal due to the much slower growth rate of Fe_3O_4. (For interpretation of the references to colour in this figure legend, the reader is referred to the web version of this article.)

Table 1
Calibrated parameters for the parabolic growth rate of FeO and Fe_3O_4.

-	$k_0 \ (m^2 s^{-1})$	$T_a \ (K)$
FeO	2.670×10^{-4}	20319
Fe_3O_4	1.027×10^{-6}	21310

calibrated via line fitting to the plotted data points as reported in Table 1.

3. Model of iron particle ignition

In the current analysis, a thermophysical model based on the mass and energy balance equations with an empirically calibrated kinetic model of iron oxidation is used to describe the ignition process of an isolated iron particle and a suspension of iron particles. The detailed formulation and major assumptions made in this model are presented this section.

3.1. Model formulation for an isolated iron particle

This model considers a spherical particle consisting of a core of iron, an inner FeO layer, and an outer Fe_3O_4 layer as illustrated in Fig. 3(a). For the temperature range over which the oxidation kinetic model is calibrated, i.e., 973 K to 1523 K, the thickness of Fe_2O_3 is about 1 % of the total thickness of the oxide film. The formation of Fe_2O_3 is thus neglected in this model. Since the thermal conductivities of Fe and FeO are greater than that of the surrounding gas by two to three orders of magnitude, a typical Biot number of a fine iron particle is on the order of $0.001 - 0.01$. Hence, a uniform particle temperature, T_p, can be assumed. The particle exchanges heat with the ambient gas at a temperature T_g via convective and radiative heat transfer. Other major assumptions on which the current model is based are summarized in the list below:

1. The densities of solid iron, FeO, Fe_3O_4 are considered as constant values, i.e., the effect of thermal expansion is neglected. Given the fact that, in the temperature range between 900K and 1200K, which is relevant to the current analysis, the coefficients of thermal expansion of Fe, FeO, and Fe_3O_4 vary over approximately the same range on the order of $1 \times 10^{-6} K^{-1}$ [54–56], oxide layer cracking due the mismatch in thermal expansion between the oxide shell and the metal core is unlikely to occur for iron particles.

2. The phase changes from α-Fe to γ-Fe and from γ-Fe to δ-Fe are not considered since the associated latent heats are much less than the specific energy release of FeO and Fe_3O_4 formation. The thermodynamic properties of iron used in the calculation are those of α-Fe.

3. Curvature effect on the oxide layer growth is neglected as the oxide layer thickness is much less than the particle radius during the ignition process.

4. The flow velocity of the ambient gas relative to the particle is negligible, i.e., the corresponding Reynolds number is zero.

The mass balance equations for Fe, FeO, and Fe_3O_4 can be related to the parabolic kinetic model (Eqs. 1 and 3) as follows,

$$\frac{dm_{Fe}}{dt} = -\nu_{Fe/FeO}\frac{dm_{FeO}}{dt} - \nu_{Fe/Fe_3O_4}\frac{dm_{Fe_3O_4}}{dt} \quad (4)$$

$$\frac{dm_{FeO}}{dt} = \rho_{FeO}A_{FeO}\frac{dX_{FeO}}{dt} = \frac{\rho_{FeO}A_{FeO}k_{0,FeO}}{X_{FeO}} \text{Exp}\left(\frac{-T_{a,FeO}}{T_p}\right) \quad (5)$$

$$\frac{dm_{Fe_3O_4}}{dt} = \rho_{Fe_3O_4}A_p\frac{dX_{Fe_3O_4}}{dt} = \frac{\rho_{Fe_3O_4}A_p k_{0,Fe_3O_4}}{X_{Fe_3O_4}} \text{Exp}\left(\frac{-T_{a,Fe_3O_4}}{T_p}\right)$$
$$(6)$$

where $\nu_{Fe/FeO}$ and ν_{Fe/Fe_3O_4} are the stoichiometric mass ratios. Note that the formation of FeO takes place at the outer surface of the FeO layer (with an area $A_{FeO} = 4\pi(r_{Fe} + X_{FeO})^2$) and the formation of Fe_3O_4 at the outer surface of the particle (with an area $A_p = 4\pi(r_{Fe} + X_{FeO} + X_{Fe3O4})^2$). The ratio between the total oxide layer thickness and particle radius, δ, and the ratio between the Fe_3O_4 layer thickness and the total oxide layer thickness, $\delta_{Fe_3O_4}$, are defined as follows:

$$\delta = \frac{X}{r_p} = \frac{X_{FeO} + X_{Fe_3O_4}}{r_p} \qquad \delta_{Fe_3O_4} = \frac{X_{Fe_3O_4}}{X} \quad (7)$$

In this analysis, the initial value of $\delta_{Fe_3O_4}$ is set to be 0.05 as inferred from experimental measurements [4,5]. Given the fact that the total thickness of the oxide layer is much thinner than the radius of the iron core, i.e., $X_0 \ll r_{Fe,0}$ and $r_{Fe,0} \approx r_{p,0}$, the initial ratio between the oxide layer thickness and the particle radius, δ_0, is approximately proportional to the initial mass fraction of the oxide layer via the follow relation:

$$\frac{m_{oxide,0}}{m_{Fe,0}} \approx \frac{4\pi r_{Fe,0}^2 X_0 \rho_{oxide}}{\frac{4}{3}\pi r_{Fe,0}^3 \rho_{Fe}} = \frac{3\rho_{oxide}X_0}{\rho_{Fe}r_{p,0}} = \frac{3\rho_{oxide}\delta_0}{\rho_{Fe}}. \quad (8)$$

where ρ_{oxide} is the average density of the oxide layer. The initial mass fraction of iron oxides is an experimentally measurable quantity.

The total enthalpy (or internal energy) of the particle H_p is the sum of the enthalpy of each solid-phase species,

$$H_p = \sum_i^{N_s} \frac{m_i h_i(T_p)}{W_i} \quad (9)$$

where N_s is the number of solid-phase species, i is the index of each species, and W_i is the molar weight of the ith species, and h_i is the corresponding molar enthalpy as a function of temperature described by the Shomate equation based on the NIST Standard Reference Data [57]. Knowing the value of H_p and m_i, particle temperature T_p can be determined via Eq. 9 following an iterative root-finding procedure. The energy balance equation of the particle tracks the rate of change in H_p as follows,

$$\frac{dH_p}{dt} = q_{FeO}\frac{dm_{FeO}}{dt} + q_{Fe_3O_4}\frac{dm_{Fe_3O_4}}{dt} - \frac{h_{O_2}(T_g)}{W_{O_2}}\frac{dm_{O_2}}{dt}$$
$$- A_p\left[h_p(T_p - T_g) + \sigma\epsilon(T_p^4 - T_g^4)\right] \quad (10)$$
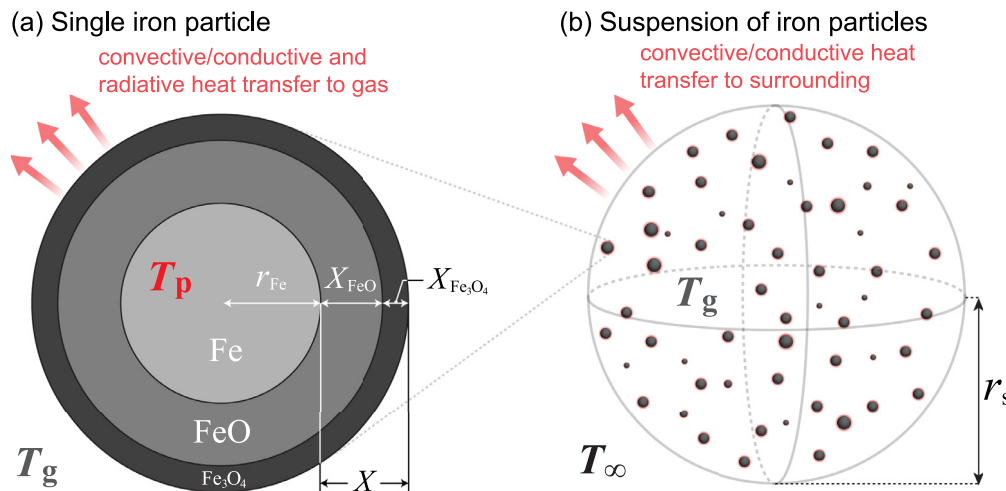
Fig. 3. Schematic of the thermophysical model of (a) an isolated particle consisting of a core of pure Fe, an inner oxide layer of FeO, and an outer oxide layer of Fe_3O_4 and (b) a spherical suspension of reacting iron particles.

The first two terms on the right-hand side of Eq. 10 are the energy release rates due to the formation of FeO and Fe_3O_4, respectively, where q_{FeO} and $q_{Fe_3O_4}$ are values of the specific energy release that are related to the enthalpy of formation H_f° of the oxide products as $q_{FeO} = -\Delta H_{f,FeO(S)}^\circ / W_{FeO}$ and $q_{Fe_3O_4} = -\Delta H_{f,Fe_3O_4(S)}^\circ / W_{Fe_3O_4}$. The third term in Eq. 10 accounts for the increase in the enthalpy of the particle due to the incorporation of the mass of gaseous oxygen[2], wherein h_{O_2} is the molar enthalpy of O_2 given by the NASA Thermodynamics Database [58]. The mass consumption rate of O_2 is calculated as follows,

$$\dot{m}_R \frac{dm_{O_2}}{dt} = -v_{O_2/FeO} \frac{dm_{FeO}}{dt} - v_{O_2/Fe_3O_4} \frac{dm_{Fe_3O_4}}{dt} \tag{11}$$

where $v_{O_2/FeO}$ and v_{O_2/Fe_3O_4} are the stoichiometric mass ratios.

The fourth and fifth terms in Eq. 10 are the rates of convective and radiative heat transfer between the particle and the ambient gas, respectively. The coefficient of convective heat transfer of the particle h_p can be determined as follows,

$$h_p = \frac{Nu\lambda_g}{d_p} \tag{12}$$

where Nu and d_p are the Nusselt number and diameter of the particle, respectively, and λ_g is the thermal conductivity of the ambient gas mixture of O_2 and an inert species (i.e., N_2, Ar, He, and Xe considered in this analysis). The thermal conductivity of each gaseous species λ_i as a function of temperature can be determined using the NASA polynomials [58]. The transport properties of the gaseous species are evaluated in the particle-gas boundary layer, T_{sf}. A "two-third law" [59,60] is used to estimate T_{sf}, i.e., $T_{sf} = (2T_p + T_g)/3$, in this paper.[3] The mixture-averaged thermal conductivity λ_g can then be calculated as follows,

$$\lambda_g = \frac{1}{2}\left(\sum_i^{N_g} X_i \lambda_i + \frac{1}{\sum_i^{N_g} X_i/\lambda_i}\right) \tag{13}$$

where N_g is the number of species in the gaseous mixture and X_i is the mole fraction of the ith species. The Nusselt number can be estimated using the Frössling (or Ranz-Marshal) correlation:

$$Nu = 2 + 0.552 Re^{\frac{1}{2}} Pr^{\frac{1}{3}}. \tag{14}$$

Table 2
Properties of Fe, FeO, and Fe_3O_4.

Property	Value	Unit
ρ_{Fe}	7874	kg m^{-3}
ρ_{FeO}	5745	kg m^{-3}
$\rho_{Fe_3O_4}$	5170	kg m^{-3}
q_{FeO}	3.787	MJ kg^{-1}
$q_{Fe_3O_4}$	4.841	MJ kg^{-1}
ϵ	0.88	-

As a result of Assumption 4, the Nusselt number equals to two (i.e., Nu = 2) for a spherical object in a quiescent medium, and thus, $h_p = \lambda_g/r_p$. Note that, although the term $h_p(T_p - T_g)$ describes the rate of convective heat transfer, it is referred to as "conductive heat loss" when discussing the results of the current analysis given the assumption of a quiescent gas medium. In the radiative heat transfer term, σ and ϵ denote the Stefan-Boltzmann constant and the emissivity of the oxide layer (Fe_3O_4) covering the particle surface, respectively. A constant value of $\epsilon = 0.88$ is considered in this analysis as the total emissivity of magnetite varies slightly from 0.85 to 0.89 as temperature increases from 773 K to 1473 K [61]. Note that, since the total emissivity of hematite varies from 0.75 to 0.85 over a range in temperature from 850 K to 1300 K [62,63], the current model may slightly overestimates the radiative heat transfer rate of an iron particle covered by a thin layer of Fe_2O_3. The values of the key properties of the solid species are provided in Table 2.

3.2. Model formulation for a suspension of iron particles

This model considers a spherical cloud of iron particles suspended in a gas mixture of O_2 and an inert species at constant pressure. The radius of this spherical suspension (denoted as r_s shown in Fig. 3) will increase as a result of thermal expansion of the gas mixture. The model monitors the mass and heat transfer between the particles and the gas mixture (as described by the model for an isolated particle in Sect. 3.1) and the heat transfer between the gas mixture and the surrounding gas at a temperature T_∞ outside the suspension. Several simplifying assumptions are made in order to better focus this study on the key parameters controlling the ignition characteristics of an iron-particle suspension:

---

[2] The negative value of the mass consumption rate of oxygen, dm_{O_2}/dt, makes the oxygen enthalpy term in the energy balance positive.

[3] Due to the fact that the difference between T_p and T_g is small during the ignition process, different ways of estimating T_{sf} does not make a significant difference in the prediction of the model.

1. A monodisperse suspension, i.e., all of the particles are of the same initial size.
2. The total volume occupied by the particles is negligible compared to the total volume of the suspension.
3. Radiative heat transfer is neglected.
4. The suspension expands freely at a constant pressure of 1 atm.
5. No slip between the expanding gas mixture and particles, i.e., the spatial distribution of particles expands with the gas mixture so that the volume of the entire suspension increases due to thermal expansion of the gas.
6. Flow velocity of the surrounding gas relative to the suspension is zero.

Knowing the initial radius of each iron particle, $r_{Fe,0}$, the initial, total mass of iron particles in a suspension, $m_{Fe,tot,0}$, can be related to the number of particles N_p as follows:

$$m_{Fe,tot,0} = \frac{4\pi N_p \rho_{Fe} r_{Fe,0}^3}{3}. \tag{15}$$

Although the overall stoichiometry of an iron-oxygen mixture is not uniquely defined, due to multiple possible oxidation states, an equivalence ratio considering FeO as the only product can be defined as follows:

$$\phi_{FeO} = \frac{m_{Fe,tot,0}/m_{O_2,0}}{2W_{Fe}/W_{O_2}}. \tag{16}$$

The initial mass of O_2 in the suspension $m_{O_2,0}$ is related to the initial temperature, $T_{g,0}$, pressure, p_0, and O_2 mass fraction $Y_{O_2,0}$:

$$m_{O_2,0} = V_{s,0}\rho_{g,0}Y_{O_2,0} = \frac{p_0 V_{s,0} Y_{O_2,0}}{\mathcal{R}_g T_{g,0}}, \tag{17}$$

where $\mathcal{R}_g$ is the specific gas constant of the gas mixture, $\rho_{g,0}$ is the initial gas density, and $V_{s,0}$ is the initial suspension volume. Thus, by specifying $T_{g,0}$, p_0, $Y_{O_2,0}$, $r_{Fe,0}$, $r_{s,0}$, and ϕ_{FeO}, one can calculate N_p, $m_{Fe,tot,0}$, and $m_{O_2,0}$ via Eqs. 15–17 as input parameters to this suspension model.

Based on the above-listed assumptions, the gas-phase energy balance equation of a suspension is formulated as follows:

$$\frac{dH_g}{dt} = N_p A_p h_p (T_p - T_g) + A_s h_s (T_\infty - T_g). \tag{18}$$

The total enthalpy of the gas mixture H_g is the sum of the enthalpies of O_2 and an inert species is,

$$H_g = \frac{m_{O_2} h_{O_2}(T_g)}{W_{O_2}} + \frac{m_I h_I(T_g)}{W_I}, \tag{19}$$

where the subscript "I" denotes the inert species (i.e., N_2, Ar, He, and Xe considered in this study). The mass balance equation of O_2 in the suspension is formulated as:

$$\frac{dm_{O_2}}{dt} = -N_p \left(\nu_{O_2/FeO} \frac{dm_{FeO}}{dt} + \nu_{O_2/Fe_3O_4} \frac{dm_{Fe_3O_4}}{dt} \right). \tag{20}$$

As the gas temperature, T_g, and the mass of O_2 change over time, the volume of the suspension changes according to the ideal gas law. Note that an isobaric condition at 1atm is considered in all of the calculations with the suspension model.

4. Sample results

4.1. An isolated particle

Sample results of the calculations considering an isolated iron particle with an initial diameter $d_{p,0} = 20$ μm and an initial oxide layer thickness $X_0 = X_{FeO,0} + X_{Fe_3O_4,0} = 10$ nm ($\delta_0 = 10^{-3}$) in air ($X_{O_2} : X_{N_2} = 0.21 : 0.79$) are plotted in Fig. 4. The subfigures (a) and (b) show the time histories of particle temperature T_p and the thicknesses of the FeO layer (solid curves) and Fe_3O_4 layer (dashed
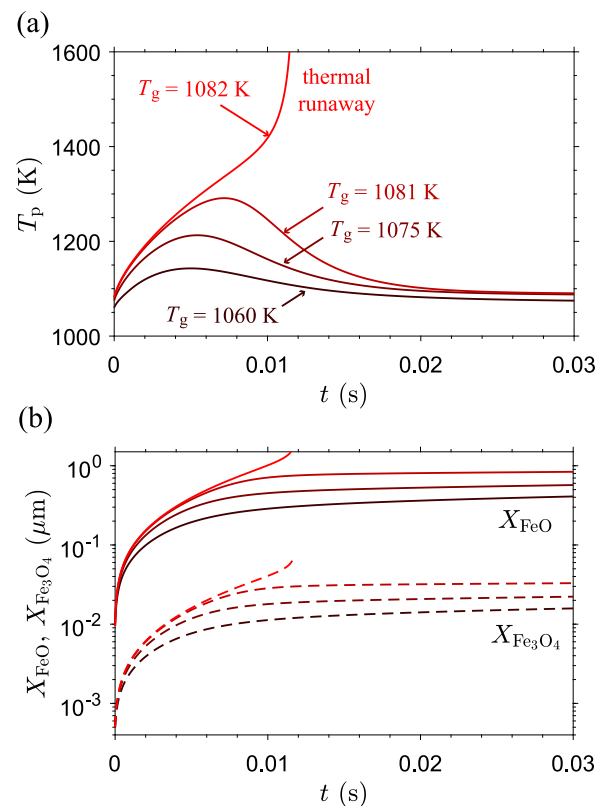

Fig. 4. Sample results showing the time histories of (a) particle temperature T_p and (b) the thicknesses of FeO layer (solid curves) and Fe_3O_4 layer (dashed curves) at four different gas temperatures (i.e., from bottom to top, $T_g = 1060$ K, 1075 K, 1081 K, and 1082 K) for an initial particle size $d_{p,0} = 20$ μm with an initial oxide layer thickness of $X_0 = X_{FeO,0} + X_{Fe_3O_4,0} = 10nm$ in air ($X_{O_2} : X_{N_2} = 0.21 : 0.79$).

curves), respectively. Each curve corresponds to a case with a different constant gas temperature T_g. Particle temperature is initialized to be equal to T_g for all of the cases. The initial thickness of the FeO layer is 95% of X_0. For the cases with $T_g \leq 1081$ K, as shown in Fig. 4(a), T_p non-monotonically varies over time, exhibiting an increase to a peak value followed by an asymptotic decrease to T_g. Figure. 4(b) shows that the oxide layer thicknesses for $T_g \leq 1081$ K reach a quasi-plateau after an initial increase until approximately 0.01 s. For the case with $T_g = 1082$ K, T_p increases monotonically with time as shown in Fig. 4(a). This increase in temperature becomes abrupt after approximately 0.01 s. The calculation was stopped once T_p reaches the melting point of FeO (i.e., 1650 K). At this stopping point, the slopes of the X_{FeO} and $X_{Fe_3O_4}$ curves (shown in Fig. 4(b)) indicate that oxide layer thicknesses continue to increase instead of asymptotically approaching a plateau value.

4.2. Suspension of particles

Sample suspension model results shown in Fig. 5 are for the cases with an initial suspension radius $r_{s,0} = 1$ cm, particle size $d_{p,0} = 20$ μm, and oxide layer thickness of $X_0 = 10$ nm in air at equivalence ratios $\phi_{FeO} = 1$, 0.25, and 0.1. The particle and gas temperatures of a suspension are initialized to be equal to the surrounding gas temperature T_∞, and are plotted as dashed and solid curves in Fig. 5, respectively. Each pair of T_p and T_g curves correspond to a case with a constant T_∞. The curve of T_p is slightly above that of T_g for all of the cases. For the cases with $\phi_{FeO} = 1$ as shown in Fig. 5(a), $T_\infty \leq 904K$, the resulting temperatures vary non-monotonically over time; for the cases with $T_\infty \geq 905K$, T_p and
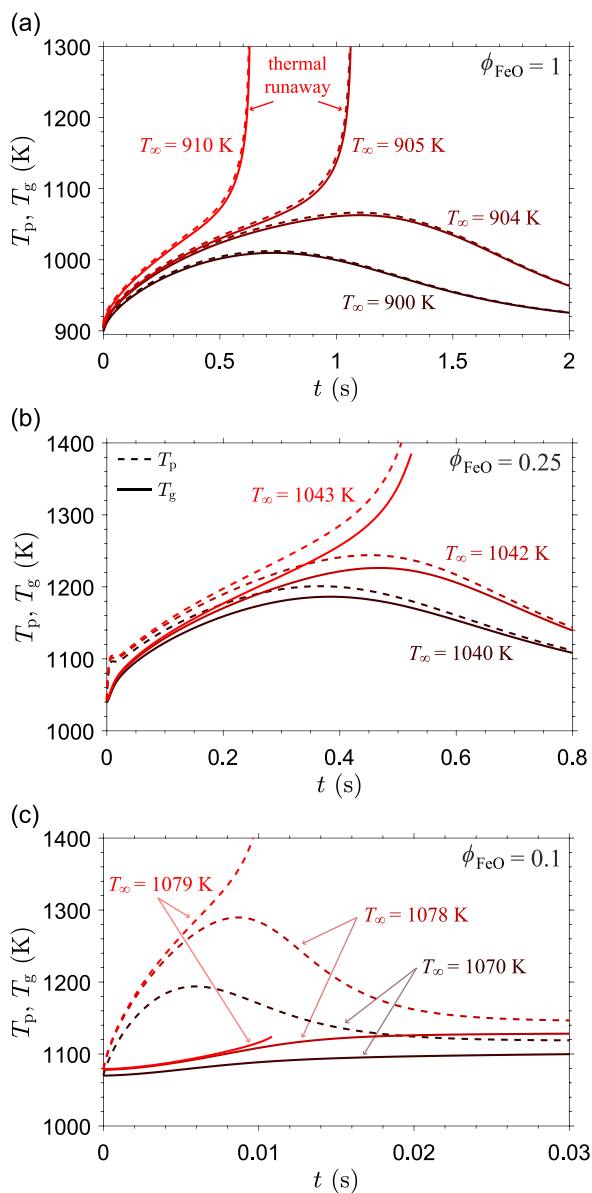
(a)

(b)

(c)

Fig. 5. Sample results showing the time histories of gas temperature T_g (solid curves) and particle temperature T_p (dashed curves) of a suspension of iron particles with an initial suspension radius $r_{s,0} = 1cm$, particle size $d_{p,0} = 20$ μm, and oxide layer thickness of $X_0 = 10nm$ in air (X_{O_2}:X_{N_2} = 0.21:0.79) at equivalence ratios (a) $\phi_{FeO} = 1$, (b) $\phi_{FeO} = 0.25$, and (c) $\phi_{FeO} = 0.1$ subjected to different surrounding gas temperatures.

T_g increase abruptly after a gradual increase over early times. For the cases with an increasingly smaller ϕ_{FeO}, the separation between T_p and T_g increases. For the cases with $\phi_{FeO} = 0.1$ as shown in Fig. 5(c), T_p increases much more rapidly than T_g does. In the case with $T_\infty = 1079K$, while T_p promptly increases, T_g slightly increases from the surrounding temperature.

5. Analysis and discussion

5.1. Critical condition of thermal runaway

A gradual increase in temperature followed by a rapid upsurge (as identified in some cases shown in Sect. 4) indicates a particle or suspension undergoing a thermal runaway. The bifurcation between the "go" and "no-go" cases is identified as a critical phenomenon of ignition. Based on the time histories resulting from
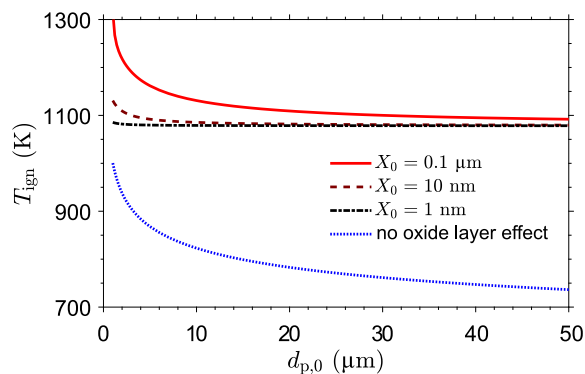

Fig. 6. Critical temperature for ignition, T_{ign}, as a function of initial particle diameter, $d_{p,0}$, with three different initial oxide layer thicknesses, i.e., $X_0 = 0.1$ μm (solid red curve), $X_0 = 10nm$ (dashed maroon curve), and $X_0 = 1nm$ (dash-dotted black curve). Results from the current model for an isolated particle in air are compared to the result of a model [60] neglecting the obstructing effect of oxide layer on the oxidation rate (plotted as the dotted blue curve). (For interpretation of the references to colour in this figure legend, the reader is referred to the web version of this article.)

the isolated particle and suspension models, critical values of T_g and T_∞ above which an isolated particle or a suspension undergoes a thermal runaway, respectively, can be determined. This critical temperature for ignition is referred to as the *ignition temperature* and denoted as T_{ign}. In this study, T_{ign} is used as a metric to probe the effects of various factors contributing to the ignition process of iron particles. Note that the radiative heat transfer term in Eq. 10 is neglected in most of the analysis shown in this section, with an exception of Sect. 5.4 wherein the effect of radiation on iron particle ignition is examined.

5.2. Effect of initial particle size and oxide layer thickness

The results of T_{ign} are plotted in Fig. 6 as a function of initial particle diameter, $d_{p,0}$, with three different initial oxide layer thicknesses for an isolated particle in air. The smallest particle size considered in this set of results is $d_{p,0} = 1$ μm. An ignition temperature significantly below the melting point of FeO is found for all particle sizes above 1 μm over a broad range of initial oxide layer thickness from 1nm to 0.1 μm. This result suggests that micron-sized or larger iron particles, which were used in most of the experimental studies on iron-fuel flames [22,24–28,35], very likely undergo an ignition process—transitioning from a kinetic-controlled reaction to an external-diffusion-controlled combustion—rather than a slow, kinetic-controlled burnout at the ambient gas temperature.

For the case with $X_0 = 0.1$ μm (the solid red curve in Fig. 6), there is a significant decrease in T_{ign} as $d_{p,0}$ increases from 1 μm to approximately 20 μm; T_{ign} nearly plateaus for further larger particles. Although qualitatively the same trend is identified for the case with a much thinner initial oxide layer of $X_0 = 10$ nm (dashed maroon curve), T_{ign} decreases less significantly with an increase in $d_{p,0}$ and reaches nearly the same plateau value (≈ 1082 K) as that resulting from the case with $X_0 = 0.1$ μm. For an even thinner initial oxide layer of $X_0 = 1$ nm (dash-dotted black curve), the entire curve of T_{ign} plateaus at 1082K, independent of initial particle size. This independence of T_{ign} on particle size (for sufficiently large particles) has been identified as a result of a parabolic oxidation rate law in Khaikin *et al.*'s [45] generic analysis of metal particle ignition, which is qualitatively explained as follows: For increasingly large particles, the increase in energy release rate (proportional to particle surface area, i.e., $\propto d_{p,0}^2$) surpasses the increase in the rate of conductive heat removal (proportional to particle size, i.e., $\propto d_{p,0}$). As a result, larger particles are more prone to ignition. If
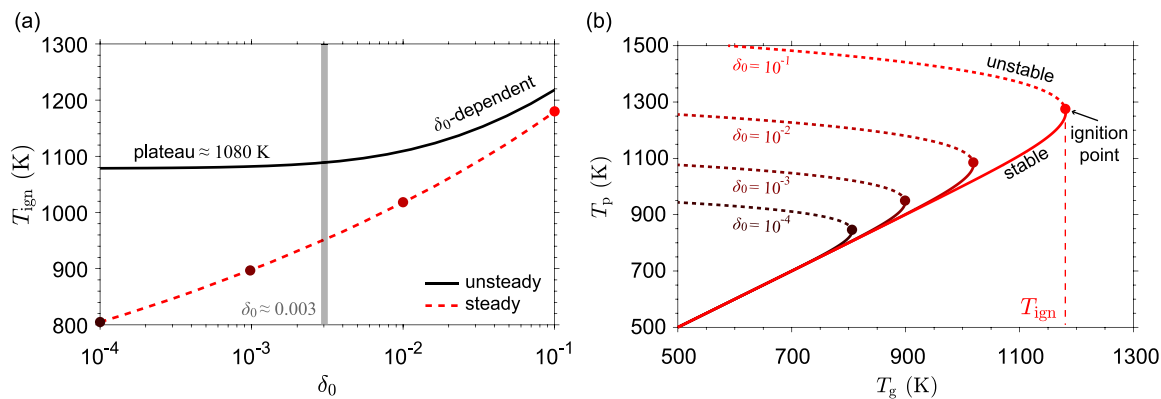
Fig. 7. (a) Ignition temperature, T_{ign}, as a function of δ_0, the ratio between initial oxide layer thickness and particle radius for an isolated iron particle in air. The results of the steady-state analysis based on the Semenov ignition criterion and the unsteady model are plotted as the dashed red curve and solid black curve, respectively. (b) The curves of T_p and T_g satisfying $\dot{q}_R = \dot{q}_L$ in the steady-state analysis with various δ_0. The turning point of each curve marks the critical condition for ignition. (For interpretation of the references to colour in this figure legend, the reader is referred to the web version of this article.)

a parabolic oxidation rate law is considered, however, to heat up larger particles requires a greater amount of energy release associated with a thicker oxide layer grown, in return, impeding the oxidation rate. Hence, a large particle size has both enhancing and hindering effects on the ignition propensity of an iron particle. These mutually compensating effects result in the independence of T_{ign} on particle size for sufficiently large particles governed by a parabolic oxidation rate law. As a comparison, the result of a model (recently proposed by Hazenberg and Oijen [60]) neglecting the impeding effect of an oxide layer on the oxidation rate is plotted as the dotted blue curve in Fig. 6. The resulting T_{ign} persistently decreases as $d_{p,0}$ increases, manifesting only the enhancing effect of an increase in particle size. Therefore, prudence must be practiced when interpreting the flame simulation results using this likely oversimplified reaction model [60].

Further analysis is performed to understand the effect of initial oxide layer thickness. The criterion for thermal runway is that the rate of energy release from iron oxidation, $\dot{q}_R$, must exceed the rate of heat loss to the surrounding gas, $\dot{q}_L$, and is formulated as follows (neglecting radiative heat transfer):

$$\dot{q}_R > \dot{q}_L$$
$$q_{FeO} \frac{dm_{FeO}}{dt} + q_{Fe_3O_4} \frac{dm_{Fe_3O_4}}{dt} > A_p h_p (T_p - T_g). \tag{21}$$

Note that the rate of energy increase due to the incorporation of gaseous oxygen (i.e., the third term on the right-hand side of Eq. 10) is also neglected in this simplified criterion. This simplification is based on the fact that the specific enthalpy associated with the incorporated O_2 is insignificant compared to the specific energy release of FeO and Fe_3O_4 formation. Considering the kinetic rate laws (Eqs. 5 and 6) and the definition of δ and $\delta_{Fe_3O_4}$ (Eq. 7), the thermal runaway criterion can be written as:

$$\tilde{q}_{FeO} \, \text{Exp}\left(\frac{-T_{a,FeO}}{T_p} \right) \frac{(1 - \delta\delta_{Fe_3O_4})^2 r_p}{\delta - \delta\delta_{Fe_3O_4}}$$
$$+ \tilde{q}_{Fe_3O_4} \, \text{Exp}\left(\frac{-T_{a,Fe_3O_4}}{T_p} \right) \frac{r_p}{\delta\delta_{Fe_3O_4}} > \lambda_g (T_p - T_g) r_p, \tag{22}$$

where $\tilde{q}_{FeO} = \rho_{FeO} q_{FeO} k_{0,FeO}$ and $\tilde{q}_{Fe_3O_4} = \rho_{Fe_3O_4} q_{Fe_3O_4} k_{0,Fe_3O_4}$. Eq. 22 shows that the energy release rates (left-hand side) and conductive heat loss rate (right-hand side) both scale linearly with particle radius, r_p. Thus, the thermal runaway criterion is independent of particle size when only conductive heat transfer is considered in the loss rate. As a result, T_{ign} exclusively depends on the initial oxide layer to particle radius ratio, δ_0, for a given gas mixture (while assuming a constant value of $\delta_{Fe_3O_4,0} = 0.05$) as shown in Fig. 7(a).

A simple steady-state analysis—neglecting the growth of the oxide layers over time—was first performed to estimate T_{ign} based on the Semenov ignition criterion (i.e., solving for T_p and T_g satisfying $\dot{q}_R = \dot{q}_L$ and $d\dot{q}_R/dT_p = d\dot{q}_L/dT_p$). The relation between T_p and T_g satisfying $\dot{q}_R = \dot{q}_L$ is plotted as the curves in Fig. 7(b) for various δ_0. Each curve exhibits a turning-point behavior. The T_p and T_g at the turning point are found as the critical condition for ignition (i.e., satisfying $d\dot{q}_R/dT_p = d\dot{q}_L/dT_p$). The branches below and above the turning point correspond to stable and unstable solutions for $\dot{q}_R = \dot{q}_L$, respectively. As shown in Fig. 7(b), the turning point or T_{ign} increases with an increase in δ_0. This steady-state analysis prediction is also plotted in Fig. 7(a) as the dashed red curve. This trend is due to the fact that reaction rate is greater for an increasingly thin oxide layer, as described by the parabolic rate law. A noteworthy finding of the steady-state analysis is that, as shown in Fig. 7(b), the ignition point can be identified for all values of δ_0 regardless of the particle size. In other words, there is no minimum size of an iron particle below which the particle cannot be ignited, i.e., ignition degenerates and the particle burnout is limited to the kinetic-controlled regime without undergoing a thermal runway or transitioning to an external-diffusion-controlled regime. This finding is in contrast to the previous work by Soo *et al.* [64], who found a minimum particle size for ignition, using a generic combustion model of metal particles that did not consider the effect of the oxide layer described by a parabolic rate law.

As shown in Fig. 7(a), T_{ign} resulting from the unsteady model, which considers the thickening of the oxide layer over time, is significantly greater than the steady-state estimation and plateaus at approximately $1080K$ for $\delta_0 \lesssim 0.003$, as indicated by the gray vertical line in Fig. 7(a). To understand this plateau behavior, the transient process of oxide-layer growth must be considered.

The time histories of particle temperature and oxide-layer growth resulting from the unsteady model for an isolated particle in air with $d_{p,0} = 20 \, \mu m$ and different initial oxide-thickness ratios subjected to two gas temperatures ($T_g = 1070$ K and $T_g = 1082$ K) are shown in Fig. 8. The subfigures (a) and (b) correspond to the cases with a gas temperature $T_g = 1070$ K that is slightly below the plateau value of $T_{ign} = 1080$ K marked in Fig. 7. None of these cases, with various δ_0, results in a thermal runaway. As shown in Fig. 8(b), δ increases the most rapidly in the case with $\delta_0 = 10^{-4}$ and collapses onto the curve of $\delta_0 = 10^{-3}$ upon reaching $\delta \approx 0.003$ (indicated by the gray horizontal line) around $t = 1 \times 10^{-4}$ s. Figures 8(c) and (d) are for the cases with $T_g = 1082$ K, which is slightly greater than the plateau T_{ign}. The cases with $\delta_0 = 10^{-4}$ and $\delta_0 = 10^{-3}$ result in a thermal runaway while the other two
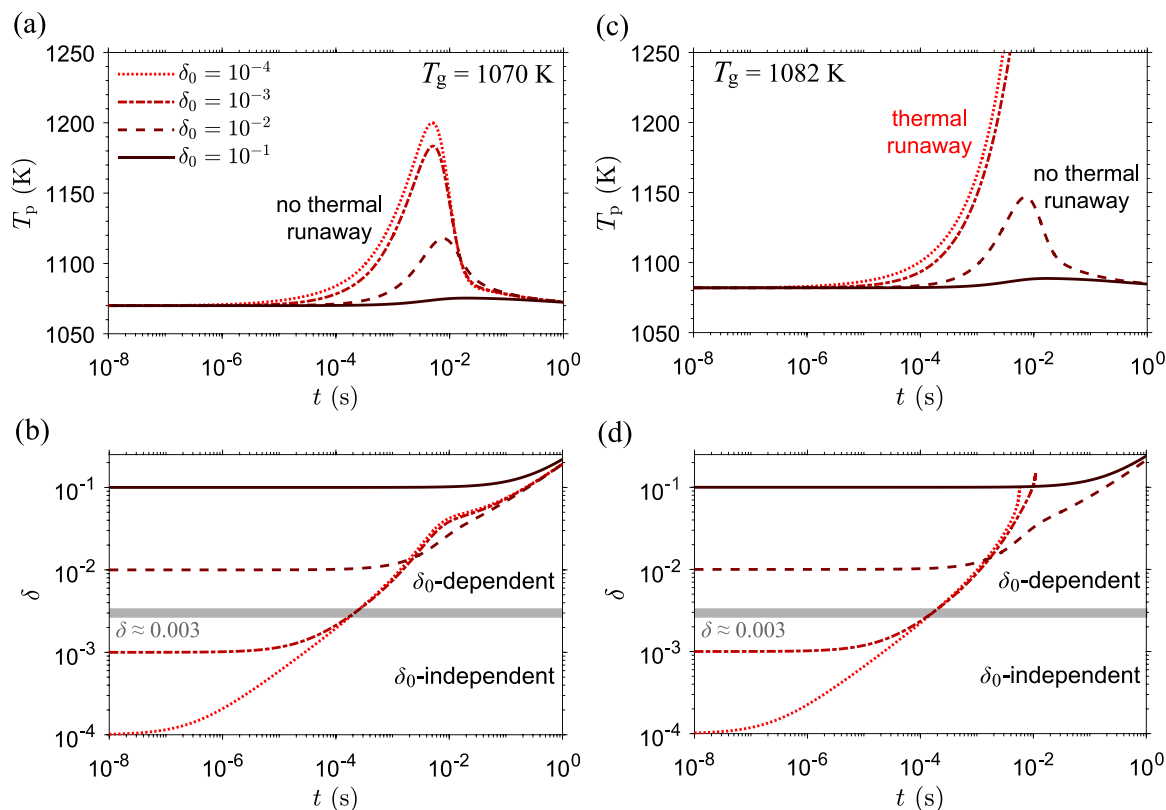
Fig. 8. The time histories of particle temperature, T_p [(a) and (c)] and the ratio between oxide layer thickness and particle radius, δ [(b) and (d)], for an isolated iron particle in air with $d_{p,0} = 20$ μm and four different initial oxide thickness ratios, i.e., $\delta_0 = 10^{-4}$ (dotted), $\delta_0 = 10^{-3}$ (dash-dotted), $\delta_0 = 10^{-2}$ (dashed), and $\delta_0 = 10^{-1}$ (solid), subjected to two gas temperatures, i.e., $T_g = 1070$ K for (a) and (b), and $T_g = 1082$ K for (c) and (d).

cases, with greater values of δ_0, do not. Note that the curves of δ for the cases with $\delta_0 = 10^{-4}$ and $\delta_0 = 10^{-3}$ shown in Fig. 8(d) are cut off because the calculations were stopped once the melting point of FeO is reached. Again, the δ growth curves for the cases with $\delta_0 = 10^{-4}$ and $\delta_0 = 10^{-3}$ collapse upon reaching $\delta \approx 0.003$ around $t = 1 \times 10^{-4}$ s. By comparing the cases with $T_g = 1070$ K and $T_g = 1082$ K, the characteristic time scale of thermal runaway is identified to be greater than 1×10^{-3} s. The order of magnitude of this time scale suggests that, for increasingly thin initial oxide layers below $\delta_0 \approx 0.003$, a rapid oxide-layer growth up to a time scale of 1×10^{-4} s has no effect on the later processes determining whether a thermal runaway occurs. For sufficiently thin initial oxide layers, T_{ign} is thus independent of δ_0.

5.3. Effect of inert gas species

The current model considers the fact that the kinetics of iron oxidation is controlled by solid-phase diffusion and is independent of gas-phase O_2 concentration (at least, for $p_{O_2} > 4 \times 10^{-4}$ atm). This means that, as the gaseous composition is varied, the ignition characteristics of an iron particle are only influenced by the change in the thermal conductivity of the ambient gas. The T_{ign} resulting from the unsteady model for an isolated particle with $\delta_0 = 10^{-3}$, in a gas mixture with O_2 and different inert species, is plotted as a function of the mole fraction of O_2 in Fig. 9. The result of T_{ign} for the case with N_2 (plotted as the solid curve) does not change significantly as X_{O_2} varies, owing to the fact that the thermal conductivities of diatomic gases O_2 and N_2 are very close. For the case with He, the resulting T_{ign} increases with a decrease in X_{O_2}. This trend is due to the fact that He has a higher thermal conductivity than that of O_2. A greater mole fraction of He thus enhances
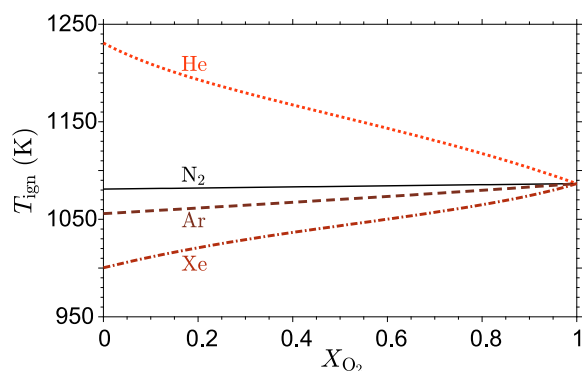

Fig. 9. The ignition temperature T_{ign} of an isolated iron particle with $\delta_0 = 10^{-3}$ as a function of mole fraction of oxygen X_{O_2} in a bulk gas mixture with different inert species, i.e., He (dotted), N_2 (solid), Ar (dashed), and Xe (dash-dotted).

the rate of conductive heat loss from the particle to the gas mixture, resulting in a greater T_{ign}. On the other hand, the T_{ign} for the cases with Ar and Xe decrease significantly as oxygen mole fraction decreases, since Ar and Xe have an increasingly low thermal conductivity. A reduced thermal conductivity of the ambient gas has a heat preserving effect on a reacting particle, thereby, facilitating thermal runaway.

5.4. Effect of radiative heat transfer

If the heat loss from a particle to the surrounding gas via radiative heat transfer is considered, the criterion of thermal runaway
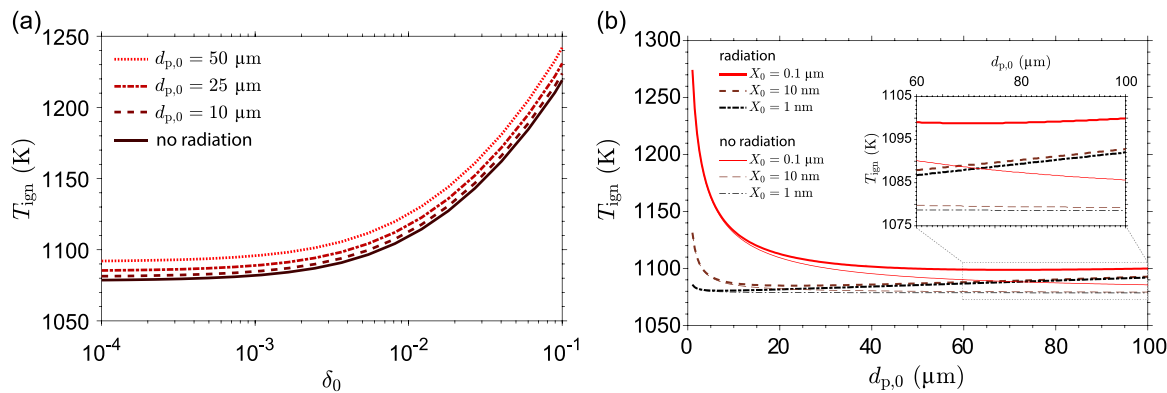
Fig. 10. The ignition temperature, T_{ign}, of an isolated iron particle of (a) different initial sizes, i.e., $d_{p,0} = 50\ \mu m$ (dotted), $d_{p,0} = 25\ \mu m$ (dash-dotted), and $d_{p,0} = 10\ \mu m$ (dashed), with radiative heat transfer to the ambient air and without radiative heat transfer (solid) plotted as a function of δ_0, and (b) different initial oxide layer thicknesses, i.e., $X_0 = 0.1\ \mu m$ (solid), $X_0 = 10 nm$ (dashed), and $X_0 = 1 nm$ (dash-dotted), with (thick curves) and without (thin curves) radiative heat transfer plotted as a function of $d_{p,0}$. The inset in (b) is a zoom-in view showing the resulting trends of T_{ign} for relatively large particles.

(formulated as Eqs. 21 and 22) is augmented as follows:

$$q_{FeO} \frac{dm_{FeO}}{dt} + q_{Fe_3O_4} \frac{dm_{Fe_3O_4}}{dt} > A_p h_p (T_p - T_g) + A_p \sigma \epsilon (T_p^4 - T_g^4)$$

$$\tilde{q}_{FeO} \operatorname{Exp}\left(\frac{-T_{a,FeO}}{T_p}\right) \frac{(1 - \delta\delta_{Fe_3O_4})^2 r_p}{\delta - \delta\delta_{Fe_3O_4}} + \tilde{q}_{Fe_3O_4} \operatorname{Exp}\left(\frac{-T_{a,Fe_3O_4}}{T_p}\right) \frac{r_p}{\delta\delta_{Fe_3O_4}}$$

$$> \lambda_g (T_p - T_g) r_p + \sigma \epsilon (T_p^4 - T_g^4) r_p^2. \tag{23}$$

Note that the radiative heat loss rate scales quadratically with particle size while the energy release rates and conductive heat loss rate scale linearly with r_p. The heat removal effect due to radiation is thus enhanced for increasingly large particles. This effect is reflected by the results of T_{ign} as a function of δ_0, for the cases with various initial particle sizes, and T_{ign} as a function of $d_{p,0}$, for the cases with different initial oxide layer thicknesses, as shown in Figs. 10(a) and (b), respectively. In Fig. 10(a), the resulting T_{ign} for the cases with radiative heat loss are greater than the T_{ign} for the case neglecting radiation (the solid curve), and increase with an increasingly large $d_{p,0}$ for all values of δ_0. For a fixed initial oxide layer thickness X_0 and relatively small particle sizes, as shown in Fig. 10(b), T_{ign} decreases as $d_{p,0}$ increases. The results for the cases with (thick curves in Fig. 10(b)) and without (thin curves) radiative heat loss are indistinguishable below approximately $d_{p,0} = 10\ \mu m$. For relatively large particles, e.g., $d_{p,0} \geq 60\ \mu m$ as shown in the inset of Fig. 10(b), T_{ign} resulting from the cases with radiative heat loss slightly increases with an increase in $d_{p,0}$ while the T_{ign} without radiation effect slightly decrease or plateau. As demonstrated by the results in Fig. 10, the difference in T_{ign} between the cases with and without radiative heat loss is less than 20 K, i.e., a relative discrepancy less than 2%, suggesting that radiative heat loss has a minor effect on the ignition characteristics of fine iron particles.

5.5. Collective heating effect in a suspension of particles

The results of T_{ign} for a spherical suspension of iron particles (with $\delta_0 = 10^{-3}$ and a fixed initial particle size of $d_{p,0} = 20\ \mu m$) in air are plotted as a function of ϕ_{FeO}, i.e., the fuel equivalence ratio considering FeO as the only oxide product in Fig. 11(a). The calculations were performed for a constant gas composition $X_{O_2}:X_{N_2} = 0.21:0.79$ while ϕ_{FeO} is varied by changing the number of particles inside the suspension according to Eqs. 15 and 16. As the initial radius of a spherical suspension increases from $r_{s,0} = 1\ mm$ (dashed curve) to 5 cm (dotted curve), the resulting T_{ign} decreases from approximately 1075 K, which is slightly below the T_{ign} for an isolated particle (indicated by the solid horizontal line), to values

below 800K. This reduction in T_{ign} is due to the collective effect of energy released by multiple particles suspended within a finite-sized volume that is losing heat to the surrounding via its external surface [64]. Analogous to an isolated particle, the conductive heat loss rate of a spherical suspension scales linearly with suspension radius as $A_s \propto r_s^2$ and $h_s \propto 1/r_s$. The rate of energy release from the reacting particles in a suspension scales with N_p that is proportional to r_s^3. The increase in energy release rate thus surpasses the increase in heat loss rate for an increasingly large suspension. This analysis suggests that, as a result of the collective effect, the critical ignition temperature of iron particles within a flame may be lower than that for an isolated particle. Future experimental effort is required to quantitatively probe the collective heating effect on flame propagation in suspensions of iron particles.

Another remark on the result shown in Fig. 11(a) is that T_{ign} monotonically decreases as ϕ_{FeO} increases. As the kinetic oxidation rate is independent of the O_2 concentration of the suspension, the overall energy release rate is not affected by a slight depletion of O_2 prior to transitioning to an external-diffusion-controlled combustion. Thus, the ignition propensity of a suspension is enhanced by an increase in volumetric concentration of iron particles, regardless of the corresponding equivalence ratio. As ϕ_{FeO} decreases to very small values, the volumetric number density of iron particles approaches zero and, thus, the resulting T_{ign} of a suspension reverts back to the value of an isolated particle.

Although T_{ign} of an isolated iron particle is independent of initial particle size for a fixed value of δ_0 (as discussed in Sect. 5.2), Fig. 11(b) shows that T_{ign} of a suspension increases with $d_{p,0}$ of individual particles for a fixed equivalence ratio $\phi_{FeO} = 1$. For a fixed iron concentration in a suspension, the smaller the particles are, the larger internal surface area is available to reaction, while the external surface area of the suspension, for heat loss into the surrounding, remains the same. Thus, smaller particles give rise to a more pronounced collective effect on enhancing the ignition propensity of a suspension. A similar enhancement due to the collective effect for smaller particles has also been identified in the ignition analysis for agglomerates of metal particles [64,65].

5.6. Transition from kinetic- to diffusion-controlled combustion

Although the current model considering a completely kinetic-controlled reaction rate is sufficient to predict the ignition temperature, for temperatures greater than T_{ign}, it can be further developed to estimate the conditions under which an iron particle transitions from a kinetic-controlled combustion to an external-
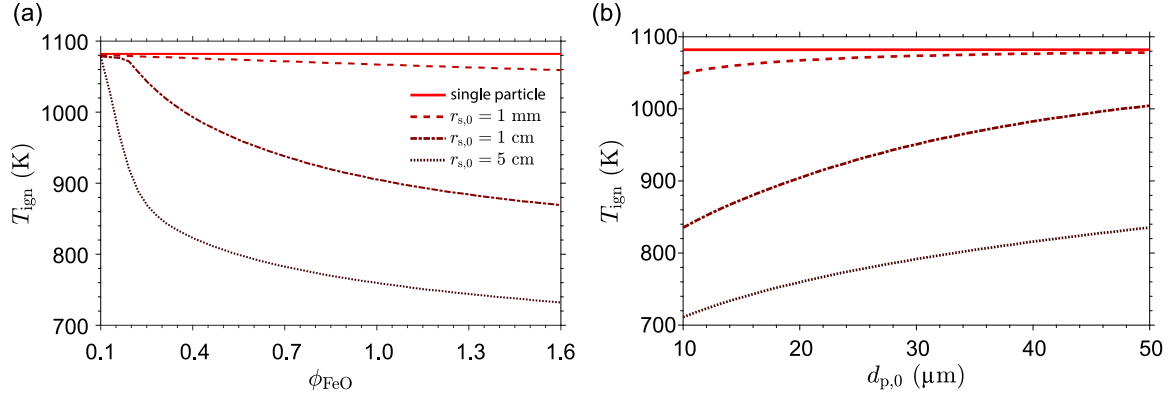
Fig. 11. The ignition temperature, T_{ign}, of a suspension of iron particles in air with different initial suspension radii, i.e., $r_{s,0} = 1$ mm (dashed), $r_{s,0} = 1$ cm (dash-dotted), and $r_{s,0} = 5$ cm (dotted), and $\delta_0 = 10^{-3}$ (a) as a function of fuel equivalence ratio (assuming FeO as the only product) with $d_{p,0} = 20$ μm and (b) as a function of initial particle diameter with $\phi_{FeO} = 1$. The value of T_{ign} for an isolated particle (with $\delta_0 = 10^{-3}$) in air is marked by the horizontal solid line.
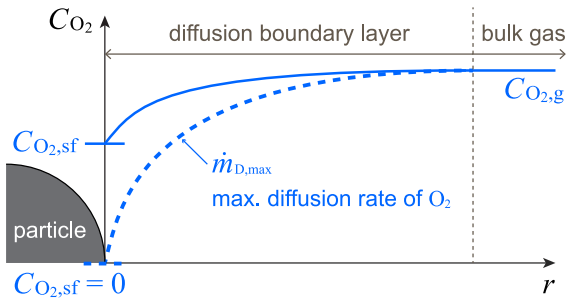
Fig. 12. Schematic illustrating the diffusion of O_2 from the bulk gas to the particle surface. The dashed curve corresponds to the case of the maximum diffusion rate at a given O_2 concentration in the bulk gas.

diffusion-controlled combustion. This further development is based on the generic $k - \beta$ paradigm [64] of particle reaction that considers the interplay between the condensed-phase (or heterogeneous) oxidation kinetics and the transport of oxidizer from the ambient gas to the particle surface. The kinetic consumption rate of O_2, denoted as $\dot{m}_R$, is governed by the parabolic rate laws of iron oxidation as described by Eq. 11. This kinetic rate is approximated to be independent of the gaseous O_2 concentration at the particle surface, $C_{O_2,sf}$, for any $C_{O_2,sf} > 0$, as justified in Sect. 2.1. The rate of O_2 mass transport, $\dot{m}_D$, from the ambient gas to the particle surface (as illustrated in Fig. 12) can be estimated as follows,

$$\dot{m}_D = A_p \beta_p (C_{O_2,g} - C_{O_2,sf}) \tag{24}$$

where $C_{O_2,g}$ and $C_{O_2,sf}$ are the concentrations of O_2 in the bulk gas and at the particle surface, respectively. The diffusive mass transfer coefficient β_p is expressed as:

$$\beta_p = \frac{Sh D_{O_2}}{d_p}. \tag{25}$$

The Sherwood number (Sh) for a spherical particle can also be calculated using the Frössling correlation:

$$Sh = 2 + 0.552 Re^{\frac{1}{2}} Sc^{\frac{1}{3}}. \tag{26}$$

Under the assumption of a quiescent gas medium, Sherwood number equals to two, thus, $\beta_p = D_{O_2}/r_p$. The diffusivity, D_{O_2}, through this diffusion boundary layer around a particle is estimated based on the mixture-averaged thermal conductivity calculated via Eq. 13 assuming a unity Lewis number. The maximum O_2 diffusion rate corresponds to the case wherein $C_{O_2,sf} = 0$ as illustrated by the dashed curve in Fig. 12 and can be calculated as:

$$\dot{m}_{D,max} = 4\pi r_p D_{O_2} C_{O_2,g}, \tag{27}$$

where D_{O_2} is a function of gas composition and particle surface temperature, T_{sf}, estimated via the two-third law based on T_p and T_g.

For $C_{O_2,sf} > 0$, the kinetic rate is less than the maximum rate of O_2 diffusion, i.e., $\dot{m}_R < \dot{m}_{D,max}$, and the O_2 consumption rate of the particle, $\dot{m}_{O_2}$, is completely controlled by the solid-phase kinetics. When $C_{O_2,sf} = 0$, the maximum O_2 diffusion rate is reached such that $\dot{m}_{O_2}$ must be equal to $\dot{m}_{D,max}$. Considering the nature of solid-phase iron oxidation, the generic $k - \beta$ model can thus be specialized to a *switch*-type model between the kinetic- and external-diffusion-controlled oxidation rates as:

$$\begin{cases} \dot{m}_{O_2} = \dot{m}_R & \text{if } \dot{m}_R < \dot{m}_{D,max} \\ \dot{m}_{O_2} = \dot{m}_{D,max} & \text{otherwise} \end{cases}, \tag{28}$$

to more accurately describe the transitions between the particle combustion regimes at temperatures greater than T_{ign}. Once a particle transitions into external-diffusion-limited combustion, the total reaction rate of O_2, $\dot{m}_{O_2}$, is partitioned into the formation rates of FeO and Fe_3O_4 based on the ratio between the kinetic rates (as shown in Fig. 2) of FeO and Fe_3O_4 formation at the corresponding T_p, X_{FeO}, and $X_{Fe_3O_4}$. Figure 13 shows the comparison between $\dot{m}_R$ (dash-dotted curve) and $\dot{m}_{D,max}$ (solid curve) resulting from the unsteady model for an isolated particle of $d_{p,0} = 20$ μm in air. When $\dot{m}_R$ exceeds $\dot{m}_{D,max}$, it indicates the transition of a particle from a kinetic-controlled to an external-diffusion-controlled combustion. The results of $\dot{m}_R$ and $\dot{m}_{D,max}$ stop when T_p reaches the melting point (m.p.) of FeO.

The results for the cases with a fixed gas temperature of $T_g = 1250$ K and various initial oxide thicknesses are plotted in Fig. 13(a)-(c), and for the cases with a fixed initial oxide thickness ratio of $\delta_0 = 10^{-3}$ and various gas temperatures are plotted in Fig. 13(d)-(f). For a relatively thin oxide layer of $\delta_0 = 10^{-3}$ and a moderately high gas temperature of 1250 K, as shown in Fig. 13(a) and (e), $\dot{m}_R$ is initially greater than $\dot{m}_{D,max}$ for a very short period of time and then decreases below $\dot{m}_{D,max}$ around $t = 10$ μs due to the growth of the oxide layer slowing down the reaction rate. Over this short period of $\dot{m}_R > \dot{m}_{D,max}$, the particle reaction rate is external-diffusion controlled. After a short oxidation phase, the oxide layer grows sufficiently that the reaction rate slows and a transition to kinetic control is observed. At a later time around $t = 2 \times 10^{-4}$ s, $\dot{m}_R$ again becomes greater than $\dot{m}_{D,max}$. This crossover marks the transition of the particle from a kinetic-controlled combustion to an external-diffusion-controlled combustion prior to reaching the melting point of FeO. This *double transition* behavior is identified in the region of thin initial oxide layer
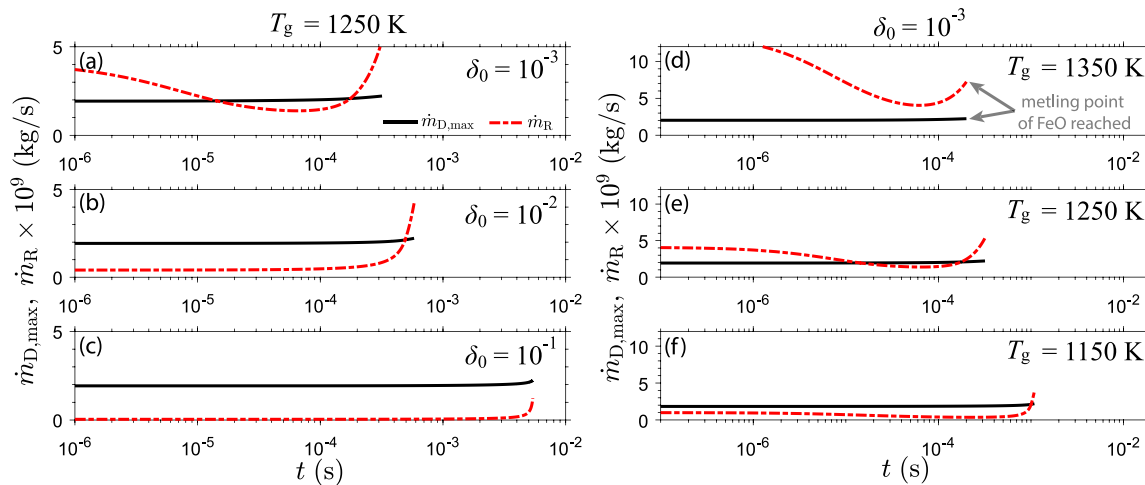
Fig. 13. Comparison between the kinetic consumption rate, $\dot{m}_R$, and the maximum external diffusion rate, $\dot{m}_{D,max}$, of O_2 in air for the cases of an initially 20μm-sized particle with (a-c) a fixed gas temperature of $T_g = 1250$ K and increasingly large initial oxide thickness ratios and (d-f) a fixed $\delta_0 = 10^{-3}$ and increasingly high gas temperatures.

and moderately high initial particle temperature (which equals to gas temperature) as marked by the orange circles ○ in Figure 14.

For a fixed gas temperature at 1250 K with a larger initial oxide thickness ratio $\delta_0 = 10^{-2}$, the particle initially burns under a kinetic-controlled regime ($\dot{m}_R < \dot{m}_{D,max}$) and transitions to a diffusion-controlled combustion shortly prior to reaching the melting point of FeO as shown in Fig. 13(b). A similar transition behavior is found for the case with a smaller initial oxide ratio $\delta_0 = 10^{-3}$ and a lower gas temperature at 1150K as shown in Fig. 13(f). In Fig. 14, the green asterisks ✳ mark the cases with a kinetic-to-diffusion transition below the melting point of FeO.

For cases with a sufficiently thin initial oxide layer and high gas temperature, e.g., $\delta_0 = 10^{-3}$ and $T_g = 1350$ K as shown in Fig. 13(d), $\dot{m}_R$ remains greater than $\dot{m}_{D,max}$ throughout the combustion process prior to the FeO melting point, suggesting that the thermal runaway process is likely to be completely controlled by the external diffusion of O_2. This scenario is identified for the cases with a thin initial oxide thickness and high gas temperature as marked by the red crosses ✕ in Fig. 14. This finding implies that, if a particle

is abruptly heated to a sufficiently high temperature without a significant growth of oxide layer (e.g., by laser heating in Ref. [36]), its ignition characteristics may not be governed by the kinetics of solid-phase iron oxidation at all.

In the case with $T_g = 1250$ K and an even thicker initial oxide layer of $\delta_0 = 10^{-1}$, $\dot{m}_R$ remains smaller than $\dot{m}_{D,max}$ throughout the entire thermal runaway process prior to reaching the FeO melting point as shown in Fig. 13(c). Thus, no transition from kinetic- to diffusion-controlled combustion occurs before the particle starts to melt. The region in the $T_{p,0} - \delta_0$ parametric space marked by the cyan plus symbols + in Fig. 14 corresponds to the cases without a transition below the melting point.

5.7. The characteristics of ignition delay time, τ_{ign}

For isolated particles with heat loss to the surrounding, ignition delay times, τ_{ign}, can be determined for the cases with a gas temperature (and initial particle temperature) equal to or greater than the ignition temperature, i.e., $T_g = T_{p,0} \geq T_{ign}$, using the augmented reaction-rate model, Eq. 28. For metal particles, since the increase of temperature is interrupted by phase changes, ignition delay time cannot be conveniently measured based on the mo-
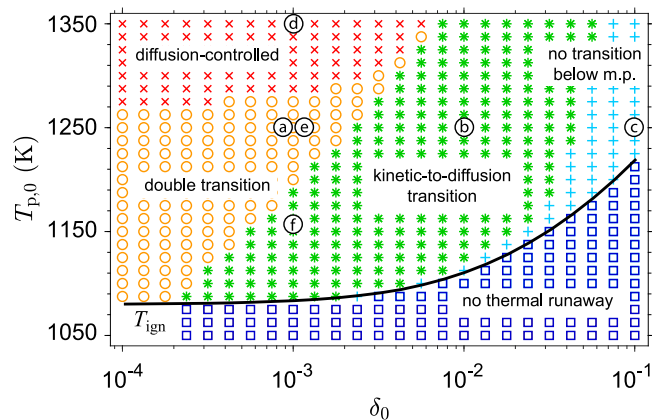

Fig. 14. A map in the parametric space of initial particle temperature $T_{p,0}$ ($= T_g$) and δ_0 summarizing different behaviors of transition (prior to the melting point of FeO) between particle combustion regimes that are identified via the comparison between $\dot{m}_R$ and $\dot{m}_{D,max}$ for the case with $d_{p,0} = 20$ μm. The different transition behaviors are marked as follows: ✕ Completely external O_2-diffusion-controlled ($\dot{m}_R > \dot{m}_{D,max}$, e.g., Fig. 13(d)); ○ transition from an initially diffusion- to kinetic-controlled regime followed by a transition from kinetic- to diffusion-controlled regime ($\dot{m}_R > \dot{m}_{D,max} \rightarrow \dot{m}_R < \dot{m}_{D,max} \rightarrow \dot{m}_R > \dot{m}_{D,max}$, e.g., Figs. 13(a) and (e)); ✳ transition from kinetic- to diffusion-controlled regime ($\dot{m}_R < \dot{m}_{D,max} \rightarrow \dot{m}_R > \dot{m}_{D,max}$, e.g., Figs. 13(b) and (f)); + completely kinetic-controlled, no transition below the melting point of FeO ($\dot{m}_R < \dot{m}_{D,max}$, e.g., Fig. 13(c)).

ment of maximum temperature increase as commonly defined for homogeneous reactive mixtures. In this study, τ_{ign} is measured as the time elapsed from the beginning of each calculation with $T_g = T_{p,0}$ to the moment when T_p reaches the melting point of FeO, i.e., 1640 K. This quantity can be measured and compared consistently in future studies. The effects of initial oxide-layer thickness and particle size on τ_{ign} of isolated particles are first examined in Sects. 5.7.1 and 5.7.2, respectively. In order to better probe the dependence of τ_{ign} on the reaction nature of iron particles, τ_{ign} is also analyzed for adiabatic suspensions of particles in Sect. 5.7.4.

5.7.1. Effect of initial oxide-layer thickness on τ_{ign} of isolated particles

For a selected initial particle size of $d_{p,0} = 20$ μm, the model prediction of τ_{ign} for isolated iron particles are plotted as color contours in the parametric space of $T_{p,0}$ and δ_0, as shown in Fig. 15(a). The predicted T_{ign} as a function of δ_0 is plotted as

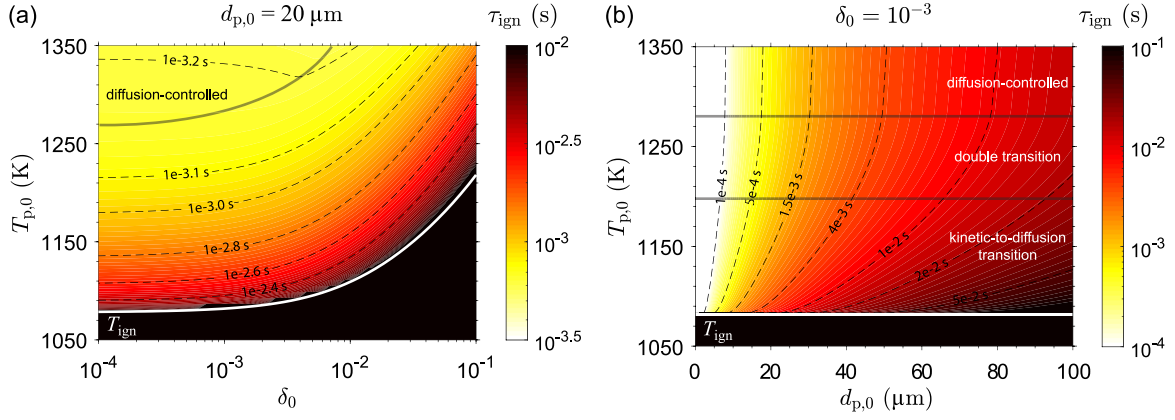**Fig. 15.** Contour plots of ignition delay time, τ_{ign}, in the parametric spaces of (a) initial particle temperature $T_{p,0}$ ($= T_g$) and δ_0 for a constant initial particle size of $d_{p,0} = 20\,\mu m$ and (b) initial particle temperature and initial particle diameter for $\delta_0 = 10^{-3}$. The white curve in each plot indicates the ignition temperature, T_{ign}. The dashed curves are the isocontours of τ_{ign}. The gray curve in (a) indicates the boundary of the completely external-diffusion-controlled regime marked by × in Fig. 14. The gray horizontal lines in (b) indicate the boundaries (in $T_{p,0}$) between the diffusion-controlled, double-transition, and kinetic-to-diffusion-controlled regimes, as identified in Fig. 14.
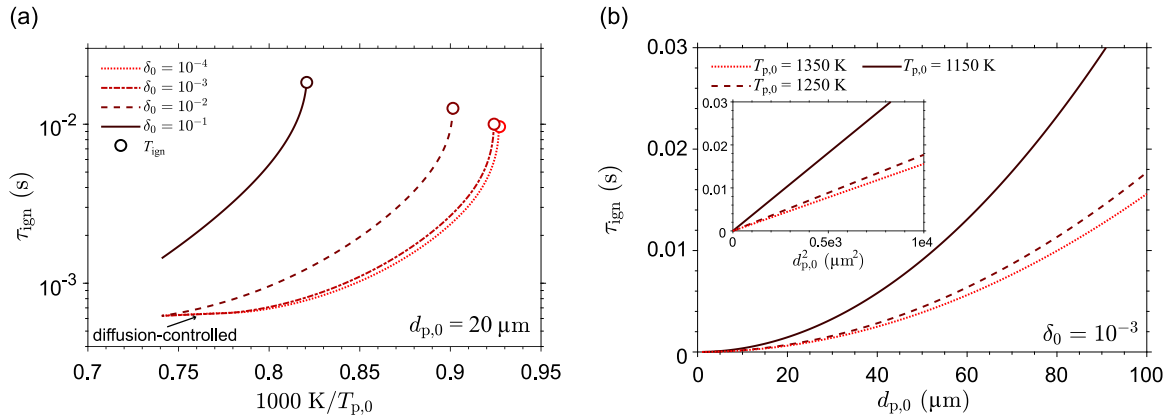

Fig. 16. The model prediction of τ_{ign} as (a) a function of the reciprocal of initial particle temperature, $T_{p,0}$, with $d_{p,0} = 20\,\mu m$ and various values of δ_0, and (b) a function of initial particle size, $d_{p,0}$, with $\delta_0 = 10^{-3}$ and various values of $T_{p,0}$. The inset of (b) shows the plot of τ_{ign} as a function of $d_{p,0}^2$.

the white curve on the color contours. The dashed curves indicate the isocontours of τ_{ign}. The gray curve indicates the boundary of the completely external-diffusion-controlled region marked by × in Fig. 14. Fig. 15(a) shows that, outside the external-diffusion-controlled region, the isocontours of τ_{ign} follow qualitatively the same trend of T_{ign} as a function of δ_0. For a fixed initial particle size, a particle with a greater δ_0 requires a higher initial temperature to result in the same ignition delay time, reflecting the temperature dependence of kinetic-controlled combustion. Inside the diffusion-controlled region, τ_{ign} barely varies with $T_{p,0}$ or δ_0.

In Fig. 15(a), it is also of interest to note that the isocontour of $\tau_{ign} = 10^{-3.2}$ s follows an opposite trend to those outside the diffusion region: For a fixed initial size, a particle with a greater δ_0 requires a lower initial temperature to result in the same ignition delay time. The turning point of the isocontour of $\tau_{ign} = 10^{-3.2}$ s is located on the boundary of the completely diffusion-controlled region, which is marked by the gray curve. This opposite trend is observed since, for a fixed particle size and temperature with an increasingly large δ_0, the heat capacity (in JK^{-1}) of the particle slightly decreases, resulting in a stronger feedback to thermal runaway.

In Fig. 16(a), the predicted τ_{ign} for the cases with $d_{p,0} = 20\,\mu m$ and various values of δ_0 are plotted as functions of the reciprocal of $T_{p,0}$. The curves for the cases with $\delta_0 = 10^{-4}$ and 10^{-3} collapse onto a nearly horizontal line at high temperatures, correspond-

ing to the diffusion-controlled regime identified in the $T_{p,0} - \delta_0$ parametric space. As $T_{p,0}$ approaches T_{ign}, marked by the circles in Fig. 16(a), τ_{ign} increases more rapidly than exponential due to an increasingly pronounced effect of heat loss from the particle to the surrounding.

5.7.2. Effect of particle size on τ_{ign} of isolated particles

Figure 15 (b) shows the contour plot of τ_{ign} in the parametric space of $T_{p,0}$ and initial particle diameter, $d_{p,0}$, for a fixed value of $\delta_0 = 10^{-3}$. Although T_{ign} is solely dependent on δ_0, as indicated by the horizontal white line in Fig. 15(b), τ_{ign} significantly increases with particle size. For the cases with $T_{p,0}$ slightly greater than T_{ign}, τ_{ign} increases over three orders of magnitude, i.e., from 10^{-4} s to 0.1s, as $d_{p,0}$ increases from 1μm to 100μm. The horizontal gray lines mark the boundaries of different regimes of particle combustion in terms of $T_{p,0}$, and show that the transition behavior between kinetic- and diffusion-controlled combustion regimes is independent of particle size. This independence is due to the fact that the kinetic rate of oxidation, $\dot{m}_R$, and the maximum diffusion rate of O_2 from the bulk gas, $\dot{m}_{D,max}$, both linearly scale with particle size, as shown below:

$$\dot{m}_R = \tilde{v}_{O_2/FeO} \, \mathrm{Exp}\left(\frac{-T_{a,FeO}}{T_p}\right) \frac{(1-\delta\delta_{Fe_3O_4})^2 r_p}{\delta-\delta\delta_{Fe_3O_4}} + \tilde{v}_{O_2/Fe_3O_4} \, \mathrm{Exp}\left(\frac{-T_{a,Fe_3O_4}}{T_p}\right) \frac{r_p}{\delta\delta_{Fe_3O_4}}$$

$$\dot{m}_{D,max} = 4\pi r_p D_{O_2} C_{O_2,g},$$

$$(29)$$

where $\tilde{v}_{O_2/FeO} = v_{O_2/FeO}\rho_{FeO}k_{0,FeO}$ and $\tilde{v}_{O_2/Fe_3O_4} = v_{O_2/Fe_3O_4}\rho_{Fe_3O_4}k_{0,Fe_3O_4}$.

As shown in Fig. 15(b), below the boundary of the completely diffusion-controlled regime at 1281 K, the isocontours of τ_{ign} (i.e., the dashed curves) show that a larger particle requires a greater initial temperature to result in the same ignition delay time. In the completely diffusion-controlled regime, the isocontours of τ_{ign} are nearly vertical, indicating that, for a fixed initial particle size, τ_{ign} very slightly depends on particle temperature. This slight dependence is owing to the temperature-dependence of the transport properties of the gaseous species near the particle surface. The contour plot in Fig. 15(b) shows that τ_{ign} significantly increases with initial particle size. This trend is further clarified in Fig. 16(b) showing τ_{ign} as functions of $d_{p,0}$ for $\delta_0 = 10^{-3}$ and different values of $T_{p,0}$. The inset of Fig. 16(b) demonstrates that τ_{ign} scales with $d_{p,0}^2$ at all of the values of $T_{p,0}$ corresponding to both kinetic- and diffusion-controlled regimes. The ignition delay time is proportional to the thermal capacity of the particle and inversely proportional to the reaction rate. As shown in Eq. 29, both kinetic- and diffusion-controlled reaction rates linearly scale with particle size. The thermal capacity of the particle scales with particle volume, i.e., $\propto d_{p,0}^3$. Thus, the scaling between τ_{ign} and particle size follows a d^2-law[4]

5.7.3. Ignition delay time of adiabatic suspensions of particles

To better examine the dependence of τ_{ign} on the reaction nature of iron particles, the model prediction of τ_{ign} for adiabatic suspensions is analyzed in this section. As the size of a spherical suspension of particles becomes sufficiently large, i.e., $r_s \to \infty$, the conductive heat transfer from the boundary of the suspension to the inert surrounding becomes negligible. An adiabatic suspension can thus be understood as an infinitely large cloud of suspended particles. The critical ignition temperature for such a suspension goes to the limit of zero. In other words, any initial temperature can trigger a thermal runaway of an adiabatic suspension. Thus, τ_{ign}, consistently defined as the time at which the particle temperature reaches the melting point of FeO, can be measured over a broad range of initial particle (and gas) temperatures.

Figure 17 (a) shows the natural logarithm of τ_{ign} predicted for adiabatic suspensions of iron particles with $d_{p,0} = 20\ \mu m$ and various values of δ_0, plotted as functions of the reciprocal of initial particle temperature, i.e., 1000 K/$T_{p,0}$. Over the entire range of temperature from 973 K to 1523 K, the predicted curve for the case with a relatively thick initial oxide layer of $\delta_0 = 10^{-1}$ follows a nearly linear trend with a slope of the activation temperature of FeO formation. This linear trend indicates that the reaction rate of the particles is kinetic-controlled during the ignition process. As δ_0 decreases from 10^{-1} to 10^{-4}, the curves of $\ln(\tau_{ign})$ vs. $1/T_{p,0}$ become increasingly nonlinear.

To understand this nonlinear trend, the kinetic rate of oxygen consumption, $\dot{m}_R$, and the maximum external-diffusion rate, $\dot{m}_{D,max}$, for the cases with $\delta_0 = 10^{-3}$ and five selected values of $T_{p,0}$ (as marked in Fig. 17(a)) across the herein studied temperature range, are compared in Fig. 17(b). At a sufficiently high temperature, e.g., Case ⑤ with $T_{p,0} = 1400$ K, the ignition process is completely diffusion-controlled, as $\dot{m}_{D,max} < \dot{m}_R$ throughout the entire process. In this completely diffusion-controlled regime, τ_{ign} becomes independent of oxide layer thickness, as shown in Fig. 17(a) that the curves of 10^{-2}, 10^{-3}, and 10^{-4} collapse. For Case ④ with $T_{p,0} = 1250$ K, the ignition process is partly diffusion-
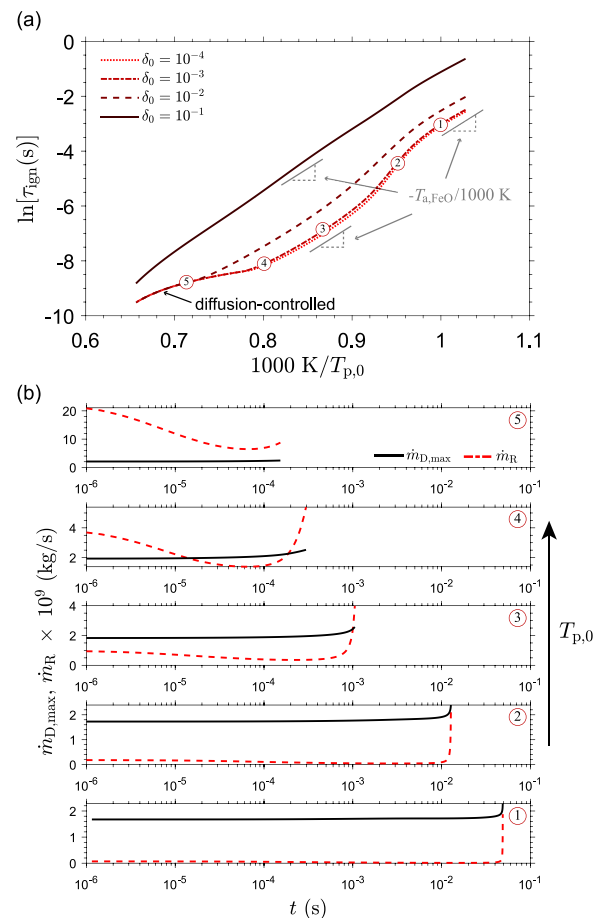
---

[4] It is of interest to note that, if the oxidation kinetics follow a linear rate law (e.g., in the generic particle combustion model proposed by Soo *et al.* [64]), $\dot{m}_R$ scales with particle surface area, i.e., $\propto d_{p,0}^2$, and thus, the scaling of τ_{ign} with particle size must follow a d-law.

Fig. 17. (a) The natural logarithm of τ_{ign} predicted for adiabatic suspensions of iron particles with $d_{p,0} = 20\ \mu m$ and various values of δ_0, plotted as functions of the reciprocal of initial particle temperature, i.e., 1000 K/$T_{p,0}$. (b) Comparison between the kinetic consumption rate, $\dot{m}_R$, and the maximum external diffusion rate, $\dot{m}_{D,max}$, of O_2 in air for the cases with $\delta_0 = 10^{-3}$ and ① $T_{p,0} = 1000$ K, ② $T_{p,0} = 1050$ K, ③ $T_{p,0} = 1150$ K, ④ $T_{p,0} = 1250$ K, and ⑤ $T_{p,0} = 1400$ K, as marked in (a).

controlled as indicated by the double-transition behavior identified in Fig. 17(b). The gradual increase in the slope of the $\ln(\tau_{ign})$-vs.-$1/T_{p,0}$ curve from Case ⑤ to Case ④, as shown in Fig. 17(a), can be attributed to this partly diffusion-controlled regime. Cases ①-③ with relatively low initial temperatures undergo a completely kinetic-controlled ignition process, as shown by the comparison between $\dot{m}_{D,max}$ and $\dot{m}_R$ plotted in Fig. 17(b). The resulting $\ln(\tau_{ign})$-vs.-$1/T_{p,0}$ curve follows a nearly linear trend with a slope of $-T_{a,FeO}$ over two separated ranges of $T_{p,0}$, which are marked by Cases ① and ③. In the intermediate temperature range marked by Case ②, τ_{ign} decreases more rapidly with an increase in $T_{p,0}$ than the slope of $-T_{a,FeO}$. This anomalous dependence of ignition delay time on temperature is likely due to the fact that τ_{ign} is measured as the time when T_p reaches a fixed temperature, i.e., the melting point of FeO. Thus, the particles with a higher initial temperature, not only have a greater kinetic reaction rate, but also require a smaller amount of energy release to reach the melting point of FeO.

5.7.4. Ignition delay time of non-adiabatic suspensions of particles

To more clearly demonstrate the collective heating effect, the model prediction of τ_{ign} as a function of ϕ_{FeO} for non-adiabatic suspensions at a common surrounding gas temperature, 1087 K, which is slightly above the T_{ign} for an isolated particle, is plotted in Fig. 18. The resulting τ_{ign} for suspensions of different initial sizes are on the same order of magnitude as τ_{ign} for an isolated

Table 3

Comparison between experimental measurements and predictions by the current model of T_{ign} of various iron (or steel) specimens.

|	T_{ign} (K)	Specimen	Conditions
Grosse & Conway, exp. [41]	1203 ± 10	10-g-weighted iron	Flow of O_2 at 1 atm
Bolobov, exp. [43]	1233 ± 20	$5 \times 5 \times 0.5$ mm low-carbon steel foil	O_2 at 0.14-0.6 MPa
Gorokhov (reviewed), exp. [39]	$588 - 1053$	Cloud of sub-mm Fe particles	Air at 1 atm
Gorokhov (reviewed), exp. [39]	$553 - 733$	Precipitated layer of sub-mm Fe particles	Air at 1 atm
Current analysis	1080	Isolated Fe particle with $\delta_0 \lesssim 0.003$	Air at 1 atm
Current analysis	$760 - 902$	Spherical suspensions of Fe particles of $d_{p,0} = 20$ μm, $\phi_{FeO} = 1$, and $r_{s,0} = 5$ cm $- 1$ cm	Air at 1 atm
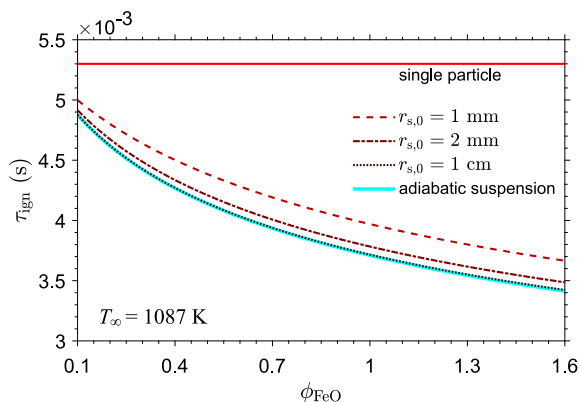
Fig. 18. The ignition delay time, τ_{ign}, of a non-adiabatic suspension of iron particles in air with different initial suspension radii and $\delta_0 = 10^{-3}$, as a function of fuel equivalence ratio (assuming FeO as the only product) with $d_{p,0} = 20$ μm at a fixed temperature 1087 K, i.e., slightly above T_{ign} for an isolated particle. The value of τ_{ign} for an isolated particle in air is marked by the horizontal solid line. The τ_{ign} for an adiabatic suspension is plotted as the thick cyan curve.

particle. For larger values of ϕ_{FeO}, τ_{ign} of suspensions becomes increasingly lower than that for an isolated particle due to a more pronounced collective heating effect. Furthermore, for a sufficiently large non-adiabatic suspension, i.e., $r_{s,0} \geq 1$ cm, the resulting τ_{ign} approaches to the values for adiabatic suspensions as indicated by the cyan curve in Fig. 18. It has been demonstrated in Sect. 5.6 that the collective heating mechanism can significantly reduce the ignition temperature of sufficiently large non-adiabatic suspensions with sufficiently high particle number densities. Note that, at a reduced T_{ign}, the ignition delay time of a suspension can be significantly longer than that of an isolated particle at its corresponding, higher, T_{ign}.

5.8. Comparison with experimental measurement

The ignition temperatures measured by Grosse and Conway [41] and Bolobov [43] for mm-sized iron specimens are perhaps the closest to the definition of T_{ign} in the current paper. In these authors' experiments, a specimen was first heated in vacuum or an inert gas to a steady and uniform temperature T_0; oxygen or air was then fed into the test chamber; the minimum T_0 triggering an abrupt increase in the temperature of the specimen, i.e., a thermal runaway, was determined as the critical temperature for ignition. The ignition temperatures reported by Grosse and Conway [41] and Bolobov [43] are 1203 ± 10 K and 1233 ± 20 K, respectively. These values are close, but slightly greater, than the range of T_{ign} predicted by the current model for an isolated iron particle in air, i.e., from 1080 K to 1220 K for $\delta_0 = 10^{-4} - 10^{-1}$ (as shown in Fig. 7). This small discrepancy can be attributed to the following reasons: (1) The iron specimens in these experiments were in direct contact with the supporting device, thus, losing heat to the surrounding via solid-phase thermal conduction; (2) a mm-

sized specimen might be subjected to a natural convection with Rayleigh number greater than unity (as considered in the analysis of Bolobov and Podlevskikh [46]); (3) the supplied oxygen flow might be of a non-negligible velocity at a lower temperature than the specimen temperature.

Bolobov [43] also found that the ignition temperature of iron is barely dependent on oxygen concentration over a broad range of p_{O_2} from 0.2 to 20 MPa. This finding is consistent with the fact that the growth rate of the FeO and Fe_3O_4 layers is controlled by the lattice diffusion of Fe ions subjected to the equilibrium Fe activities at the interlayer boundaries, and not significantly affected by the ambient O_2 concentration. Thus, the consideration of O_2-concentration-independent kinetic rates in the current analysis is supported by this experimental evidence.

As reviewed by Gorokhov [39], the experimentally measured ignition temperatures for clouds of sub-mm-sized iron particles scatter over a range from 588 K to 1053 K. This significant reduction in ignition temperature from those measured for isolated iron specimens [41–43] is likely due to the collective effect as captured by the current suspension model and discussed in Sect. 5.5. However, it is of importance to note that, since the values of the kinetic parameters (in Table 1) are only valid for iron oxidation over a temperature range from 973 K to 1523 K, the current model prediction below this range might not be quantitatively accurate.

Another possible source of inaccuracy is rooted in the assumption of spherical particles made in this study. Pulverized sponge iron (PSI) particles, e.g., those used for combustion experiments by Tóth *et al.* [35], have irregular shapes and porous structures. Iron particles produced by the reduction of spherical iron-oxide particles are porous because the iron oxides take up more volume than iron due to the fact that the Pilling-Bedworth ratios for Fe → Fe_2O_3, Fe_3O_4, and FeO are all greater than unity. An irregularly shaped, porous iron particle has a greater surface area that has access to and can react with oxygen. Thus, the ignition temperature might be significantly reduced. Future efforts are required to quantitatively measure the porosity of reduced iron particles and estimate how particle porosity enhances the ignition of particles and their suspensions.

It is noteworthy that, in reality, the oxidation rate of iron is governed by different processes when the oxide layer is extremely thin, i.e., under approximately 20 nm. The parabolic rate law considered in this analysis is based upon the assumption that Fe-cation diffusion across a sufficiently thick oxide layer with a uniform electric field is the rate-limiting process. However, for a very thin oxide layer, its growth is governed by ionic transfer driven by a large electric field and space charges in the oxide layer [53]. In this thin-layer regime, the oxidation process is better explained by the theory of Cabrera and Mott [66]. As a quantitatively reliable rate law for thin-layer growth of iron oxidation is not available, the thick-layer parabolic rate law is extrapolated in the current analysis to a thin-layer regime. The question arises as to how this extrapolation affects the accuracy in estimating the ignition characteristics of iron particles. An example of the growth rate of NiO as a function of oxide layer thickness in both thin- and thick-layer regimes is provided in Fig. 7 of Atkinson's review [53]: If one extrapolates

the parabolic rate law (Wagner's model) to nano-scale thicknesses, the growth rate would be underestimated compared to the prediction of Cabrera and Mott's model. An underestimation of the initial oxide-layer growth rate in the current analysis for iron is unlikely to have a significant effect on T_{ign}. As demonstrated in Fig. 8(b) and (d) and discussed in Sect. 5.3, for a sufficiently thin initial oxide layer, the initial rapid oxide-layer growth has no effect on the subsequent processes determining whether a thermal runaway occurs. Therefore, the thin layer mechanisms described by the theory of Cabrera and Mott, which result in greater oxidation rates over a time period much shorter than the thermal-runway time scale of an iron particle, are unlikely to have a significant effect on the ignition characteristics.

A recent study by Senyurt and Dreizin [67] demonstrates that, if the size of a reactive metal particle is comparable to the molecular mean free path of the surrounding gas, the transport processes between the particle and the gas are hindered by the rarefaction effects in the Knudsen transition regime. These authors' analysis shows that, owing to a reduced rate of heat loss to the surrounding in the Knudsen transition regime, the ignition temperatures of sufficiently small particles are significantly lower than the model prediction based upon a continuum assumption. However, this analysis is limited to a steady-state model and not applied to study iron particles. A detailed, unsteady analysis of how the ignition characteristics of fine iron particles differ in the Knudsen transition regime will be reported in a future publication.

6. Concluding remarks

A model describing the heat and mass balance equations for heterogeneously burning micrometric iron particles was developed. The solid-phase oxidation kinetics described by a parabolic rate law were empirically calibrated using measured experimental data on the time-evolution of the growth of iron-oxide layers. The model was applied to quantitatively analyze the dependence of the minimum gas temperature required for a thermal runaway (namely, the ignition temperature) on particle size, initial thickness of the oxide layer, gas-phase composition, heat loss by radiation, and the collective heating effect in particle suspensions. Findings showed that the ignition temperature depends on the ratio between the initial oxide layer thickness and particle size, δ_0, and is independent of particle size. For isolated iron particles in air, the predicted ignition temperature plateaus at approximately 1080K, and becomes independent of δ_0, for $\delta_0 \lesssim 0.003$. The lower the thermal conductivity of the gas-phase environment, the lower the ignition temperature. The ignition behavior was found to be largely independent of radiative heat loss effects. The collective heating effect in burning particle suspensions was shown to significantly reduce the ignition temperature. The slight underestimation of the ignition temperature in the current model compared to experimental literature [41,43], is likely associated with experimental conditions that facilitated further heat loss from the iron specimens in addition to convective and radiative heat loss.

The time histories of the reaction rate of the particles were used to parametrically probe the transition behavior between kinetic-controlled and external-diffusion-controlled combustion regimes. The ignition delay time is significantly influenced by the initial oxide layer thickness and particle temperature under a kinetic-controlled combustion regime; once a particle transitions to an external-diffusion-controlled regime, its ignition delay time becomes nearly independent of δ_0 and $T_{p,0}$. Furthermore, the scaling of the ignition delay time of iron particles with particle size follows a d^2-law. Future experimental and modeling efforts should work to elucidate the rate of heat release in iron particle combustion in liquid-phase, and to explore how to ensure a non-volatile combustion of molten iron droplets.

References

[1] D.B. Beach, A.J. Rondinone, B.G. Sumpter, S.D. Labinov, R.K. Richards, Solid-State combustion of metallic nanoparticles: new possibilities for an alternative energy carrier, J. Energy Resour. Technol. 129 (1) (2006) 29–32, doi:10.1115/1.2424961.

[2] J.M. Bergthorson, S. Goroshin, M.J. Soo, P. Julien, J. Palecka, D.L. Frost, D.J. Jarvis, Direct combustion of recyclable metal fuels for zero-carbon heat and power, Appl. Energy 160 (2015) 368–382, doi:10.1016/j.apenergy.2015.09.037.

[3] J.M. Bergthorson, Recyclable metal fuels for clean and compact zero-carbon power, Prog. Energy Combust. Sci. 68 (2018) 169–196, doi:10.1016/j.pecs.2018.05.001.

[4] J. Païdassi, Sur la cinetique de l'oxydation du fer dans l'air dans l'intervalle $700 - 1250°C$, Acta Metall. 6 (3) (1958a) 184–194, doi:10.1016/0001-6160(58)90006-3.

[5] J. Païdassi, Sur l'oxydation du protoxyde de fer dans l'air dans l'intervalle $600 - 1350°C$, Acta Metall. 6 (3) (1958b) 219–221, doi:10.1016/0001-6160(58)90014-2.

[6] G.J. Yurek, J.P. Hirth, R.A. Rapp, The formation of two-phase layered scales on pure metals, Oxid. Met. 8 (5) (1974) 265–281, doi:10.1007/BF00609944.

[7] W.W. Smeltzer, D.J. Young, Oxidation properties of transition metals, Prog. Solid State Chem. 10 (1975) 17–54, doi:10.1016/0079-6786(75)90003-5.

[8] G. Garnaud, R.A. Rapp, Thickness of the oxide layers formed during the oxidation of iron, Oxid. Met. 11 (4) (1977) 193–198, doi:10.1007/BF00606543.

[9] J. Sato, K. Sato, T. Hirano, Fire spread mechanisms along steel cylinders in high pressure oxygen, Combust. Flame 51 (1983) 279–287, doi:10.1016/0010-2180(83)90106-2.

[10] T. Hirano, J. Sato, Fire spread along structural metal pieces in oxygen, J. Loss Prev. Process Ind. 6 (3) (1993) 151–157, doi:10.1016/0950-4230(93)85003-4.

[11] T.A. Steinberg, G.P. Mulholland, D.B. Wilson, F.J. Benz, The combustion of iron in high-pressure oxygen, Combust. Flame 89 (2) (1992) 221–228, doi:10.1016/0010-2180(92)90030-S.

[12] T.A. Steinberg, J. Kurtz, D.B. Wilson, The solubility of oxygen in liquid iron oxide during the combustion of iron rods in high-pressure oxygen, Combust. Flame 113 (1) (1998) 27–37, doi:10.1016/S0010-2180(97)00165-X.

[13] N.R. Ward, T.A. Steinberg, The rate-limiting mechanism for the heterogeneous burning of cylindrical iron rods, J. ASTM Int. 6 (6) (2009) 1–13, doi:10.1520/JAI102269.

[14] M. Muller, H. El-Rabii, R. Fabbro, Laser ignition of bulk iron, mild steel, and stainless steel in oxygen atmospheres, Combust. Sci. Technol. 186 (7) (2014) 953–974, doi:10.1080/00102202.2014.892363.

[15] M. Muller, H. El-Rabii, R. Fabbro, Liquid phase combustion of iron in an oxygen atmosphere, J. Mater. Sci. 50 (9) (2015) 3337–3350, doi:10.1007/s10853-015-8872-9.

[16] C. Wagner, Beitrag zur theorie des anlaufvorgangs, Zeitschrift für Physikalische Chemie 21B (1) (1933) 25–41, doi:10.1515/zpch-1933-2105.

[17] K. Hauffe, The Mechanism of Oxidation of Metals—Theory, Springer US, Boston, MA, 1965, pp. 79–143.

[18] E.L. Dreizin, Phase changes in metal combustion, Prog. Energy Combust. Sci. 26 (1) (2000) 57–78, doi:10.1016/S0360-1285(99)00010-6.

[19] T. Hirano, K. Sato, Y. Sato, J. Sato, Prediction of metal fire spread in high pressure oxygen, Combust. Sci. Technol. 32 (1–4) (1983) 137–159, doi:10.1080/00102208308923656.

[20] H. El-Rabii, K.A. Kazakov, M. Muller, Experimental and theoretical study of iron and mild steel combustion in oxygen flows, Phys. Fluids 29 (3) (2017) 037104, doi:10.1063/1.4977746.

[21] J.H. Sun, R. Dobashi, T. Hirano, Combustion behavior of iron particles suspended in air, Combust. Sci. Technol. 150 (1–6) (2000) 99–114, doi:10.1080/00102200008952119.

[22] F.D. Tang, S. Goroshin, A.J. Higgins, Modes of particle combustion in iron dust flames, Proc. Combust. Inst. 33 (2) (2011) 1975–1982, doi:10.1016/j.proci.2010.06.088.

[23] P. Julien, S. Whiteley, S. Goroshin, M.J. Soo, D.L. Frost, J.M. Bergthorson, Flame structure and particle-combustion regimes in premixed methane-iron-air sus-

pensions, Proc. Combust. Inst. 35 (2) (2015) 2431–2438, doi:10.1016/j.proci.2014.05.003.

[24] A. Wright, A.J. Higgins, S. Goroshin, The discrete regime of flame propagation in metal particulate clouds, Combust. Sci. Technol. 188 (11–12) (2016) 2178–2199.

[25] M. McRae, P. Julien, S. Salvo, S. Goroshin, D.L. Frost, J.M. Bergthorson, Stabilized, flat iron flames on a hot counterflow burner, Proc. Combust. Inst. (2018), doi:10.1016/j.proci.2018.06.134.

[26] J. Palečka, J. Sniatowsky, S. Goroshin, A.J. Higgins, J.M. Bergthorson, A new kind of flame: observation of the discrete flame propagation regime in iron particle suspensions in microgravity, Combust. Flame 209 (2019) 180–186, doi:10.1016/j.combustflame.2019.07.023.

[27] J. Palečka, S. Goroshin, A.J. Higgins, Y. Shoshin, P. de Goey, J.-R. Angilella, H. Oltmann, A. Stein, B. Schmitz, A. Verga, S. Vincent-Bonnieu, W. Sillekens, J.M. Bergthorson, Percolating reactiondiffusion waves (PERWAVES)sounding rocket combustion experiments, Acta Astronaut 177 (2020) 639–651, doi:10.1016/j.actaastro.2020.07.033.

[28] N.I. Poletaev, M.Y. Khlebnikova, Combustion of iron particles suspension in laminar premixed and diffusion flames, Combust. Sci. Technol. 0 (0) (2020) 1–22, doi:10.1080/00102202.2020.1812588.

[29] F.D. Tang, A.J. Higgins, S. Goroshin, Effect of discreteness on heterogeneous flames: propagation limits in regular and random particle arrays, Combust. Theor. Model. 13 (2) (2009) 319–341.

[30] F.D. Tang, A.J. Higgins, S. Goroshin, Propagation limits and velocity of reaction-diffusion fronts in a system of discrete random sources, Phys. Rev. E 85 (2012) 036311.

[31] S. Goroshin, F.D. Tang, A.J. Higgins, Reaction-diffusion fronts in media with spatially discrete sources, Phys. Rev. E 84 (2) (2011) 027301.

[32] X. Mi, A.J. Higgins, S. Goroshin, J.M. Bergthorson, The influence of spatial discreteness on the thermo-diffusive instability of flame propagation with infinite lewis number, Proc. Combust. Inst. 36 (2) (2017) 2359–2366.

[33] F. Lam, X.C. Mi, A.J. Higgins, Front roughening of flames in discrete media, Phys. Rev. E 96 (2017) 013107, doi:10.1103/PhysRevE.96.013107.

[34] F.Y.K. Lam, X.C. Mi, A.J. Higgins, Dimensional scaling of flame propagation in discrete particulate clouds, Combust. Theor. Model. 0 (0) (2019) 1–24, doi:10.1080/13647830.2019.1703044.

[35] P. Tóth, Y. Ögren, A. Sepman, P. Gren, H. Wiinikka, Combustion behavior of pulverized sponge iron as a recyclable electrofuel, Powder Technol. 373 (2020) 210–219, doi:10.1016/j.powtec.2020.05.078.

[36] D. Ning, Y. Shoshin, J.A. van Oijen, G. Finotello, L.P.H. de Goey, Burn time and combustion regime of laser-ignited single iron particle, Combust. Flame 230 (2021) 111424, doi:10.1016/j.combustflame.2021.111424.

[37] J. Huang, S. Li, W. Cai, Y. Qian, E. Berrocal, M. Aldén, Z. Li, Quantification of the size, 3d location and velocity of burning iron particles in premixed methane flames using high-speed digital in-line holography, Combust. Flame 230 (2021) 111430, doi:10.1016/j.combustflame.2021.111430.

[38] D. Ning, Y. Shoshin, M. van Stiphout, J. van Oijen, G. Finotello, P. de Goey, Temperature and phase transitions of laser-ignited single iron particle, Combust. Flame 236 (2022) 111801.

[39] Y.M. Gorokhov, On the pyrophoric properties, explosion hazard, and toxicity of powders and dusts of iron and its compounds, Soviet Powder Metall. Metal Ceramic. 3 (1) (1964) 82–86, doi:10.1007/BF00774331.

[40] V.V. Leshchevich, O.G. Penyazkov, A.V. Fedorov, A.V. Shul'gin, J.C. Rostaing, Conditions and delay time of ignition of iron microparticles in oxygen, J. Eng. Phys. Thermophys. 85 (1) (2012) 148–154, doi:10.1007/s10891-012-0632-y.

[41] A.V. Grosse, J.B. Conway, Combustion of metals in oxygen, Ind. Eng. Chem. 50 (4) (1958) 663–672, doi:10.1021/ie50580a040.

[42] V.I. Bolobov, A.Y. Berezin, P.F. Drozhzhin, A.S. Shteinberg, Ignition of compact stainless steel specimens in high pressure oxygen, Combust. Explosion Shock Waves 27 (3) (1991) 263–266, doi:10.1007/BF00789654.

[43] V.I. Bolobov, Conditions for ignition of iron and carbon steel in oxygen, Combust. Explosion Shock Waves 37 (3) (2001) 292–296, doi:10.1023/A:1017523922778.

[44] A.L. Breiter, V.M. Mal'tsev, E.I. Popov, Models of metal ignition, Combust. Explos Shock Waves 13 (4) (1977) 475–485, doi:10.1007/BF00744795.

[45] B.I. Khaikin, V.N. Bloshenko, A.G. Merzhanov, On the ignition of metal particles, Combust. Explosion Shock Waves 6 (4) (1970) 412–422.

[46] V.I. Bolobov, N.A. Podlevskikh, Numerical analysis of conditions for ignition of compact metal specimens and foil in oxygen, Combust. Explos. Shock Waves 37 (6) (2001) 655–663, doi:10.1023/A:1012976013806.

[47] R.Y. Chen, W.Y.D. Yeun, Review of the high-temperature oxidation of iron and carbon steels in air or oxygen, Oxid. Met. 59 (5) (2003) 433–468, doi:10.1023/A:1023685905159.

[48] F. Li, Z. Sun, S. Luo, L.S. Fan, Ionic diffusion in the oxidation of ironeffect of support and its implications to chemical looping applications, Energy Environ. Sci. 4 (2011) 876–880, doi:10.1039/C0EE00589D.

[49] L. Himmel, R.F. Mehl, C.E. Birchenall, Self-diffusion of iron in iron oxides and the wagner theory of oxidation, JOM 5 (6) (1953) 827–843, doi:10.1007/BF03397553.

[50] A.G. Goursat, W.W. Smeltzer, Kinetics and morphological development of the oxide scale on iron at high temperatures in oxygen at low pressure, Oxid. Met. 6 (2) (1973) 101–116, doi:10.1007/BF00614658.

[51] D.J. Young, High temperature oxidation and corrosion of metals, volume 1, Elsevier, 2008.

[52] P. Kofstad, Nonstoichiometry, diffusion, and electrical conductivity in binary metal oxides (1972).

[53] A. Atkinson, Transport processes during the growth of oxide films at elevated temperature, Rev. Mod. Phys. 57 (1985) 437–470, doi:10.1103/RevModPhys.57.437.

[54] R.E. Carter, Thermal expansion of mgfe2o4, feo, and mgo· 2feo, J. Am. Ceram. Soc. 42 (7) (1959) 324–327.

[55] G.R. Holcomb, A review of the thermal expansion of magnetite, Mater. High Temp. 36 (3) (2019) 232–239.

[56] Y.M. Kozlovskii, S.V. Stankus, The linear thermal expansion coefficient of iron in the temperature range of 130–1180 k, Journal of Physics: Conference Series, volume 1382, IOP Publishing (2019), p. 012181.

[57] M. Chase, NIST-JANAF Thermochemical tables, 4th edition, American Institute of Physics, -1, 1998.

[58] B.J. McBride, Coefficients for calculating thermodynamic and transport properties of individual species, volume 4513, NASA Langley Research Center, 1993.

[59] G.L. Hubbard, V.E. Denny, A.F. Mills, Droplet evaporation: effects of transients and variable properties, Int. J. Heat Mass Transf. 18 (9) (1975) 1003–1008, doi:10.1016/0017-9310(75)90217-3.

[60] T. Hazenberg, J.A. van Oijen, Structures and burning velocities of flames in iron aerosols, Proc. Combust. Inst. 38 (3) (2021) 4383–4390, doi:10.1016/j.proci.2020.07.058.

[61] G.K. Burgess, R.G. Waltenberg, The emissivity of metals and oxides: Measurements with the micropyrometer, volume 11, US Department of Commerce, Bureau of Standards, 1915.

[62] Y.S. Touloukian, D.P. DeWitt, Thermophysical properties of matter - the TPRC data series. Volume 8. Thermal radiative properties - nonmetallic solids, Technical Report, Purdue University, Lafayette, IN, 1972.

[63] J.M. Jones, P.E. Mason, A. Williams, A compilation of data on the radiant emissivity of some materials at high temperatures, J. Energy Inst. 92 (3) (2019) 523–534, doi:10.1016/j.joei.2018.04.006.

[64] M. Soo, X.C. Mi, S. Goroshin, A.J. Higgins, J.M. Bergthorson, Combustion of particles, agglomerates, and suspensions - a basic thermophysical analysis, Combust. Flame 192 (2018) 384–400, doi:10.1016/j.combustflame.2018.01.032.

[65] X.C. Mi, S. Goroshin, A.J. Higgins, R. Stowe, S. Ringuette, Dual-stage ignition of boron particle agglomerates, Combust. Flame 160 (11) (2013) 2608–2618, doi:10.1016/j.combustflame.2013.06.004.

[66] N. Cabrera, N.F. Mott, Theory of the oxidation of metals, Rep. Prog. Phys. 12 (1) (1949) 163–184.

[67] E.I. Senyurt, E.L. Dreizin, At what ambient temperature can thermal runaway of a burning metal particle occur? Combust. Flame 236 (2022) 111800.